Nuclear Instruments and Methods in Physics Research A 606 (2009) 608–636

Contents lists available at ScienceDirect

Nuclear Instruments and Methods in Physics Research A

journal homepage: www.elsevier.com/locate/nima

Design and performance considerations for perforated semiconductor thermal-neutron detectors

J.K. Shultis, D.S. McGregor *

S.M.A.R.T. Laboratory, Department of Mechanical and Nuclear Engineering, 3002 Rathbone Hall, Kansas State University, Manhattan, KS 66506-2503, USA

A R T I C L E I N F O

Article history:
Received 19 January 2009
Accepted 14 February 2009
Available online 6 March 2009

Keywords:
Semiconductor neutron detectors
Solid state neutron detectors

A B S T R A C T

Perforated silicon structures backfilled with either ^{10}B or ^{6}LiF are presently under construction as high efficiency thermal-neutron detectors. Although many perforated structures are possible, there are three fundamental designs that are studied in the present work, namely (a) cylindrical perforations where holes are filled with neutron reactive material, (b) pillar configurations where semiconductor pillars are surrounded by neutron reactive material, and (c) trench structures where the trenches are filled with neutron reactive material. From results of Monte Carlo simulations, it is found that the trench structure affords the best efficiencies, exceeding 20% using conservative geometries, and over 35% for more aggressive structures. Simulated spectroscopic features and manufacturing constraints are presented and discussed.

© 2009 Elsevier B.V. All rights reserved.

1. Introduction

Semiconductor radiation detectors composed of diode devices coated with neutron reactive films have been studied for decades [1]. Material choice requires a strong neutron absorbing reactive coating that emits ionizing reaction products, preferably charged particles rather than photons. There are many strong neutron absorbers with large absorption cross sections, yet only a few of these choices spontaneously emit ionizing radiation in the form of charged particles. Typically, the neutron reactive material covering the diodes is natural Gd, ^{10}B or ^{6}LiF.

The thermal-neutron (2200 m/s) capture cross section for ^{157}Gd is 240,000 b, which permits efficient absorption of thermal neutrons in a thin film of material. Natural Gd, which has a ^{157}Gd natural abundance of 15.7%, has a thermal-neutron capture cross section of 46,000 b. However, only 60% of thermal-neutron captures result in the release of a conversion electron, thereby, reducing the effective thermal-neutron cross section of natural Gd to 27,600 b. The (n,γ) reactions yield numerous low energy conversion electrons, with a general distribution ranging from 29 up to 246 keV. However, the largest yields are from conversion electrons with energies near 70 keV, with all other energy emissions above 85 keV having much lower branching efficiencies [2]. As a result, the reaction products from Gd are mostly low energy conversion electrons which can easily be confused with background gamma-ray or beta-particle interactions. For this reason, Gd coatings are generally not used as a converter for coated semiconductor neutron detectors.

The $^{10}B(n,\alpha)^{7}Li$ neutron reaction yields two possible de-excitation branches from the excited ^{11}B compound nucleus, namely

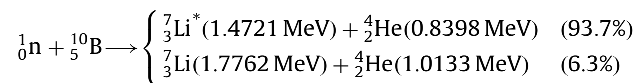

$$ {}^{1}_{0}n + {}^{10}_{5}B \longrightarrow \begin{cases} {}^{7}_{3}Li^{*}(1.4721\,MeV) + {}^{4}_{2}He(0.8398\,MeV) & (93.7\%) \\ {}^{7}_{3}Li(1.7762\,MeV) + {}^{4}_{2}He(1.0133\,MeV) & (6.3\%) \end{cases} $$

where the Li ion in the 93.7% branch is ejected in an excited state, which deexcites through the emission of a 480 keV gamma ray. For thermal neutrons, the two charged particle reaction products are ejected in opposite directions. Fully enriched ^{10}B has a 2200-m/s microscopic absorption cross section of 3840 b. With a mass density of 2.15 g/cm^3, the solid structure of ^{10}B has a macroscopic 2200-m/s neutron absorption cross section of 500.5 cm^{-1}. The absorption cross section for ^{10}B follows a $1/\nu$ dependence [3,4]. ^{10}B has been used successfully as a neutron conversion mechanism on semiconductor diodes for over 45 years, and has been used in the first demonstration of perforated diode structures [5].

The $^{6}Li(n,t)^{4}He$ neutron reaction yields a single product branch,

$$ {}^{1}_{0}n + {}^{6}_{3}Li \longrightarrow {}^{3}_{1}H(2.7276\,MeV) + {}^{4}_{2}He(2.0553\,MeV) $$

For thermal neutrons, the charged particle reaction products are ejected in opposite directions. The reaction products from the $^{6}Li(n,t)^{4}He$ reaction are more energetic than those of the $^{10}B(n,\alpha)^{7}Li$ or $^{157}Gd(n,\gamma)^{158}Gd$ reactions and, hence, are much easier to detect and discriminate from background radiations. ^{6}Li has a relatively large microscopic 2200-m/s neutron absorption

* Corresponding author. Fax: +1 785 532 4093.
E-mail address: mcgregor@ksu.edu (D.S. McGregor).
URL: http://www.mne.ksu.edu/research/centers/SMARTlab (D.S. McGregor).

0168-9002/$ - see front matter © 2009 Elsevier B.V. All rights reserved.
doi:10.1016/j.nima.2009.02.033

cross section of 940 b. The absorption cross section for ^{6}Li also follows a $1/v$ dependence [3,4]. Although devices have been fabricated with enriched ^{6}Li metal as the converter film [6], pure Li is highly reactive and is difficult to prevent from decomposing, even with encapsulation. It is the stable compound LiF that is more often used. The mass density of ^{6}LiF is 2.54 g/cm^3, and the resulting macroscopic 2200-m/s neutron absorption cross section is 57.5 cm^{-1}.

The advantages of coated diodes as neutron detectors include compact size, a low power requirement, use of low cost VLSI mass production, and ruggedness. Yet, because basic *planar* thin-film coated diode detectors have a maximum thermal-neutron detection efficiency of only about 4.5% [6], they have seen only modest use. However, recent advances with high-aspect ratio deep etching (HARDE) techniques have permitted perforated semiconductor neutron detectors to be fabricated that have much higher efficiencies. In these detectors the diode is permeated with perforations which are backfilled with neutron reactive materials, such as ^{10}B and ^{6}LiF. The first such devices were fabricated from GaAs Schottky barrier diodes, and demonstrated only modest increases in efficiency over planar diode counterparts [5], yet did demonstrate that the concept was feasible. Calculations for designs using trenches and cylindrical holes indicate that intrinsic thermal-neutron detection efficiencies above 25% can be achieved with perforated diodes, more than 5 times that of a common planar thin-film coated diode [7]. Recent work also promotes the concept of using Si pillars surrounded by ^{10}B instead of trenches and holes, with the interesting claim that such a device might achieve thermal-neutron detection efficiencies exceeding 75% [8]. As will be shown, such a claim is an exaggeration and pillar devices of the proposed design dimensions in Ref. [8] simply cannot achieve efficiencies greater than 40% under the best conditions.

In this work, three perforation designs (holes, pillars, trenches) are analyzed using Monte Carlo simulations to determine the effect that the size, depth, and geometry of the perforations have on the performance of such detectors. In particular, the energy deposition spectra and the thermal-neutron detection efficiencies of these neutron detectors are investigated.

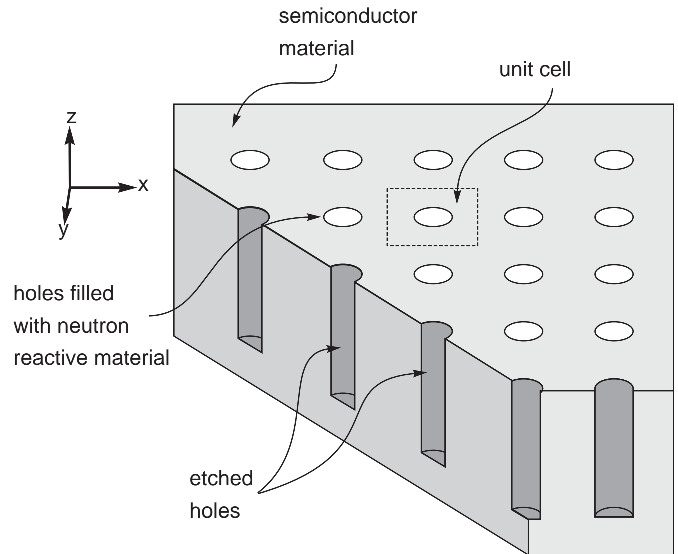

Fig. 1. The basic concept for a cylindrical hole perforated diode with the holes backfilled with neutron reactive material. Also shown is a unit cell for the structure.

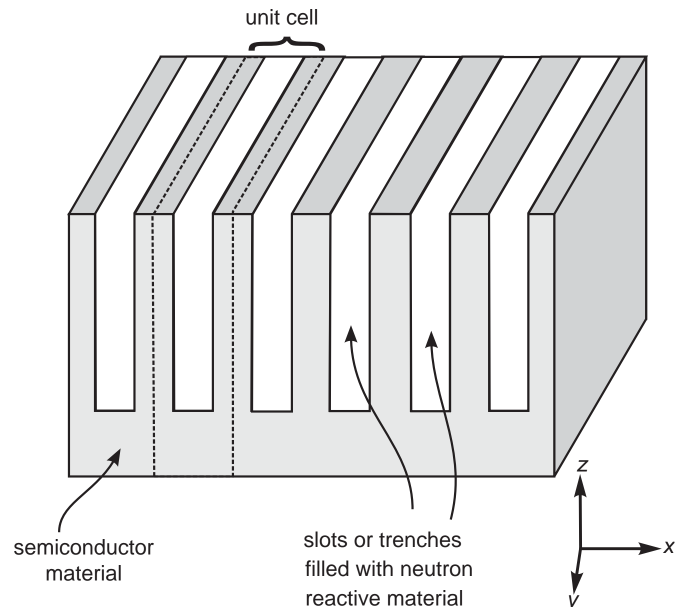

Fig. 2. The basic concept for a straight trench perforated diode with the trenches backfilled with neutron reactive material. Also shown is a unit cell for the structure.

2. Calculational considerations

Monte Carlo simulations have been used earlier to predict the performance of a perforated diode as a function of absorber material, hole diameter and depth, hole pitch, and "cap" layer thickness [7]. Here an extension is made to treat all three perforation geometries shown in Figs. 1–3 based on the unit cell for each geometry.

A plane parallel 2200-m/s neutron beam, perpendicular to the detector face, is assumed to uniformly illuminate the face of a unit cell. The silicon semiconductor material is assumed transparent to these neutrons, because neutron scattering effects in the thin silicon substrate are negligible and, hence, need not be considered. The total cross section for the converter material is taken as the ion-producing cross section. Although not presented in this study, the effect of non-normal neutron incidence is also of interest [9].

The square unit cell for the rod and pillar designs is replicated many times in the x and y directions to form a detector. The unit cell for the trench design is replicated many times in the x direction. However, only a single unit cell is used in the simulations. Reaction ions produced in the cell are tracked through the cell using specularly reflecting lateral surfaces (surfaces parallel to the z-axis) to simulate an infinite array of unit cells. As ions are tracked through the unit cell and reflected at the lateral surfaces, the energy deposited in the silicon and the neutron reactive material is calculated. After many simulated neutron-induced ion-production reactions, the spectrum of the energy deposited in the silicon is obtained. The fraction of neutrons incident on the unit cell that lead to the deposition of energy in the silicon above some lower level discriminator (LLD) setting and that, thus, produce a neutron "count" then yields the detector efficiency for the given LLD.

2.1. Monte Carlo simulations of ion energy deposition

By sampling uniformly over the illuminated surface of the detector, a random point (x_i, y_i) for a neutron incident on the detector surface is determined. Then along a ray through this

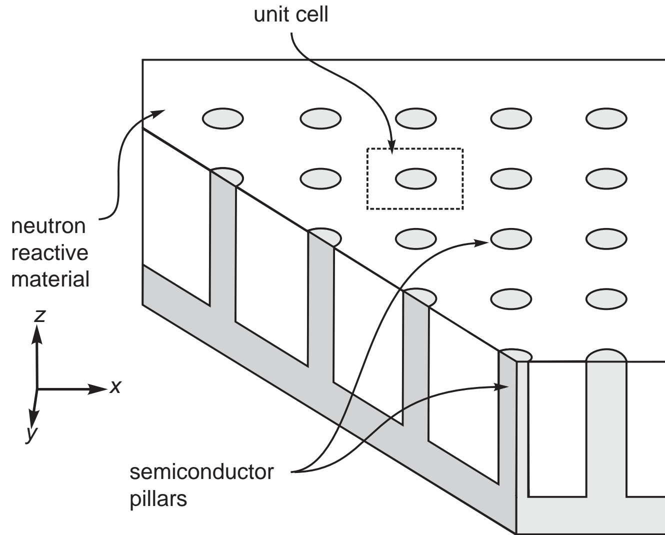

Fig. 3. The basic concept for a pillar diode with the pillars surrounded by neutron reactive material. Also shown is a unit cell for the structure.

entry point, a random depth z_i for a neutron interaction in the converter material is obtained by sampling from the distribution $f(z) = C\exp(-\Sigma z)$ where Σ is the 2200-m/s macroscopic cross section for the converter material. Here $C = [1 - \exp(-\Sigma T)]^{-1}$ is a normalization constant to make $f(z)$ a properly normalized probability distribution function. The depth T is the length of the ray through the converter material. If no converter material is in the path of the neutron ray ($T = 0$) then the neutron passes through the detector without interaction. Once a random interaction site (x_i, y_i, z_i) is determined, a random direction $\mathbf{\Omega}_i$ for one of the ions is selected from an isotropic directional distribution. The other reaction ion is then given the opposite direction $-\mathbf{\Omega}_i$. Finally, the identity of the ions is randomly selected according to the branching ratio of the various ions produced in the neutron interaction. The two ions are then tracked along their paths in the unit cell, reflected at the lateral surface of the unit cell, and "killed" if they reach the surface of the unit cell. The energy transferred to the active silicon semiconductor region along the ion tracks is then calculated.

The estimation of the energy deposited in the active silicon region is greatly simplified if all ions are assumed to travel in straight lines, i.e., scattering events and energy straggling can be neglected. For the energies of the ions considered here, a straight-line slowing-down trajectory is a good approximation [10]. Calculation of the energy deposited in the various regions of the detector is then simply a matter of computing the length of the geometric segments an ion travels in each material encountered along its straight-line path from the ion's point of birth to where it is stopped or killed. The energy deposited in the silicon by each simulated ion history is then found by calculating the energy lost by the ion over every path segment it travels in the silicon.

The energy deposited in the silicon, E_d, for a given path segment depends on the length s of the straight-line path segment in the silicon, the ion type i, and the ion-energy upon entering the silicon E. Such a function $E_d^i(E,s)$ is complicated and generally not known. To avoid having to know $E_d^i(E,s)$ a simpler *back-tracking* method is used that requires far simpler empirical functions.

To calculate the energy lost by an ion over each of its path segments by the back-tracking method, two empirical functions are needed. The first $E_m^i(s)$ is the mean residual energy after an ion of type i travels a distance s in material m from its point of birth. To obtain this function, the TRIM code [11] was used to obtain a detailed tabulation of the mean residual energy of the various ions produced by thermal-neutron interactions in the converter material (^{6}LiF or ^{10}B) as a function of path length in the converter material and in silicon. Then the TableCurve [12] computer program was used to find an empirical fit to these data. In this way accurate empirical formulas were found for $E_m^i(s)$ that permitted rapid evaluation of an ion's residual energy. The second function needed for the present Monte Carlo calculations is $S_m^i(E)$, which gives the path length in material m for the ith ion to obtain a mean residual energy E. This function is the inverse of $E_m^i(s)$. With the previous TRIM data, empirical fits for $S_m^i(E)$ were obtained. The function $S_m^i(E)$ also gives the mean range R_m^i of the ith ion in material m, namely $R_m^i = S_m^i(0)$. Also if $s > R_m^i$ then $E_m^i(s) = 0$. With these two empirical fits for $E_m^i(s)$ and $S_m^i(E)$, the energy deposited by an ion along any straight-line segment in any of the cell regions can be obtained as follows.

Consider an ion that leaves a region composed of material 1 with energy E_1 and enters an adjacent region composed of material 2. The ray in the direction of the ion travel is assumed to have a segment length s_2 in the second region, i.e., the distance from the point where the ion enters the second region to the point where the ray intersects another region or is killed when its reaches the top boundary. The problem is to estimate the energy deposited along s_2 and the residual ion energy E_2 (if any) at the end of its path in the second region. Clearly, if the ion with an initial energy E_1 in material 2 has a range less than s_2, the energy deposited in the second region is $E_d = E_1$ because $E_2 = 0$. However, if this range is greater that s_2, then $E_2 > 0$ and the deposited energy is $E_d = E_1 - E_2$.

To calculate E_2 at the end of the ray in the second medium, the trajectory is first tracked backwards to find the ion's starting position, *if the material of the regions traversed by the ion before entering the second region were replaced by the material of the second medium*, that would produce the same residual energy E_1 at the interface. This back-tracked distance is $s_1 = S_2^i(E_1)$. The energy E_2 after a path length $s_1 + s_2$, all in the material of medium 2, is simply $E_2 = E_2^i(s_1 + s_2)$. In this manner the energy deposited along the path segment s_2 is evaluated as $E_d = E_1 - E_2$. The same approach can be used to evaluate the energy lost by the ion over any path segment.

The energy the two reaction ions deposit in the silicon regions along their tracks is then recorded in an appropriate bin or tally vector for each simulated reaction event. After performing this simulation for several million reactions, an ideal energy-deposition spectrum is thus obtained. Further, the fraction of neutron histories that deposited energy greater than some minimal amount, as given by the LLD setting, gives the detector efficiency for producing a pulse or count.

2.2. Simulation of measured spectra

The spectra obtained by Monte Carlo simulations described above are ideal in the sense that no energy straggling, large-angle ion scattering or detector noise and resolution effects are considered. To simulate expected multi-channel analyzer measured spectra, which include such non-ideal effects, the ideal spectra are postprocessed to introduce a Gaussian averaging or smearing of the counts in each energy bin of the idealized spectra. The number of counts $\widehat{N}_j$ in channel j of the smeared spectrum is given by [13]

$$\widehat{N}_j = \sum_{i=1}^{N_{\max}} N_i W_{ij} \tag{1}$$

where N_i is the number of counts in the ith channel of the idealized spectrum and $N_{\max}$ is the maximum number of MCA

energy bins. Here W_{ij} are the elements of the *spreading vector*, namely,

$$W_{ij} = W_{ji} = W_{|i-j|} \equiv \frac{1}{\sqrt{2\pi}\sigma}\int_{E_j-\Delta}^{E_j+\Delta} \exp\left[-\frac{1}{2}\left(\frac{E_i - E'}{\sigma}\right)^2\right] dE' = \frac{1}{2}\left\{\mathrm{erf}\left(\frac{E_j+\Delta-E_i}{\sqrt{2}\sigma}\right) - \mathrm{erf}\left(\frac{E_j-\Delta-E_i}{\sqrt{2}\sigma}\right)\right\}. \quad (2)$$

Here E_i is the midpoint energy of MCA energy bin i with width 2Δ and σ is the standard deviation of the smoothing Gaussian. For the simulated spectra presented here, a standard deviation of $\sigma = 20\,\text{keV}$ is used. This value has been found to produce spectra typical of those measured for film-coated devices [6].

3. Perforation cases

Three basic designs are investigated here: (1) a square matrix of cylindrical hole perforations etched into the semiconductor substrate (the "hole design" of Fig. 1), (2) a design with straight and parallel trenches etched into the semiconductor substrate (the "trench design" of Fig. 2), and (3) one where a large perforation has been etched into the semiconductor leaving behind a square matrix of cylindrical semiconductor pillars (the "pillar design" of Fig. 3). In all designs the etched perforations are backfilled with neutron reactive material. There are numerous other possible perforation configurations and patterns. However, these three basic patterns demonstrate the expected performance of similar designs with slightly varying patterns.

3.1. Cylindrical hole shaped perforations

The hole design has been extensively investigated [5,7,14]. This design offers a high probability of sensing ionizing reaction products, provided the hole diameter is less than the cumulative ranges of both product ions. Shown in Fig. 4 are the basic possible trajectories that reaction ions from either the $^{10}B(n,\alpha)^7Li$ or $^6Li(n,t)^4He$ reactions may follow. In trajectory (1), the particles are emitted longitudinally along the perforation and do not enter into the semiconductor; hence they would not be recorded. However, trajectories (2) and (3), and variants, would result in one or both particles entering into the semiconductor and, thus, possibly record a count. Should an event occur in which the distance between holes is shorter than an ion's range, then the particle may enter into another hole and thereby deposit less energy in the semiconductor, as depicted in trajectory (3). The probability of these various trajectories and resultant energy deposition are a function of the fill material, hole diameter and cell pitch.

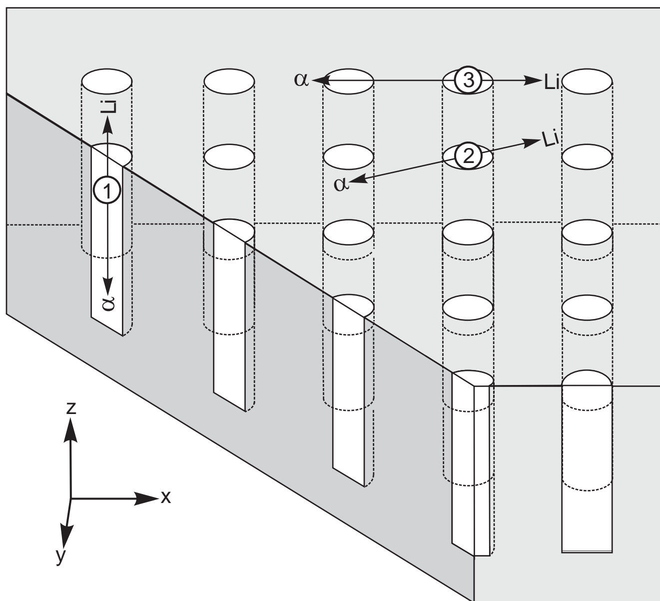

Fig. 4. There are many trajectories for reaction products in a perforated hole structure. The main trajectories of interest are shown here: (1) a complete miss occurs if the ions travel in the z direction, (2) one or both ions are absorbed in the semiconductor, and (3) with small dimensions, one or both ions can reach another absorber (^{10}B, ^6LiF) column, which effectively causes some ion energy to be lost (i.e., not absorbed in the semiconductor).

3.1.1. Efficiencies for ^{10}B filled holes

Considered here are unit cells with pitches of 4, 8, and 12 μm and with the hole depths of 10, 20, 40 and 60 μm. In the present case, the holes were backfilled with ^{10}B with a 2200-m/s macroscopic cross section of $500.5\,\text{cm}^{-1}$. The semiconductor is silicon with a mass density of $2.33\,\text{g/cm}^3$ and a Z of 14.

Shown in Fig. 5 are the computed detection efficiencies as a function of the LLD setting for the cases in which the unit cell is 4 μm wide and the holes are 2 μm in diameter (50% of the unit cell dimension). The zero LLD setting produces the highest possible efficiency, ranging from 7.6% thermal-neutron detection efficiency (ε_{tn}) for 10-μm-deep holes to 18.3% for 60-μm-deep holes. The hole design produces a fairly consistent response to thermal neutrons from LLD = 0 to 600 keV, dropping only to 6.9% for 10-μm-deep holes and only to 17.0% for 60-μm-deep holes. This result implies that the detector would operate with fairly constant efficiency provided that the LLD is set between 0 and 600 keV. Because neutrons are often accompanied by a gamma-ray background, such robustness is important to allow discrimination against background induced events.

Shown in Fig. 6 are the efficiencies as a function of the LLD setting for a unit cell of 8 μm width and with holes 4 μm in diameter (again 50% of the unit cell dimension). The efficiencies range from 7.1% for 10-μm-deep holes up to 17.0% for 60-μm-deep holes. Here the efficiencies noticeably decrease as the LLD is increased. The decrease is a consequence of the hole diameter, in which appreciable energy self-absorption can occur in the ^{10}B before the particle enters the semiconductor. As a result, the energy-deposition spectra from the device will have more counts in the lower energy channels than for those of the previous case and, hence a larger percentage of counts will be discarded as the LLD is increased.

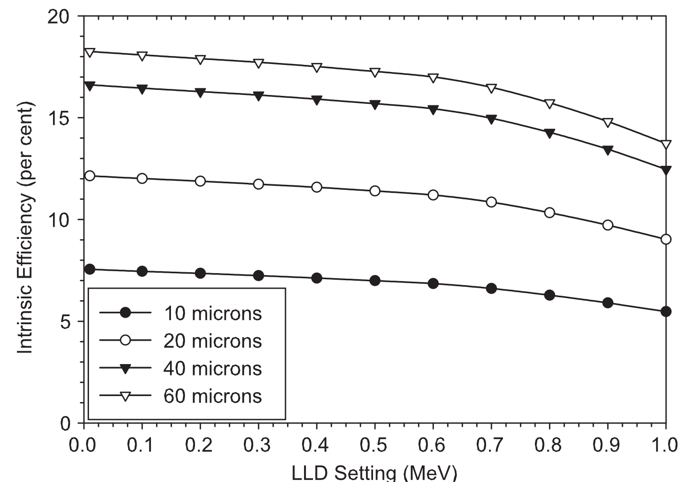

Fig. 5. Comparison of intrinsic efficiencies for different perforation depths for the cylindrical hole design. The unit cell width is 4 μm with 2-μm-diameter holes backfilled with ^{10}B.

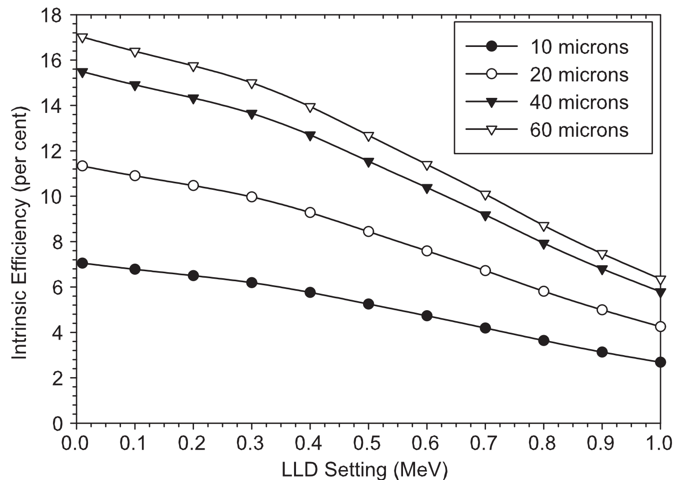

Fig. 6. Comparison of intrinsic efficiencies for different perforation depths for the cylindrical hole design. The unit cell width is 8 μm with 4-μm-diameter holes backfilled with ^{10}B.

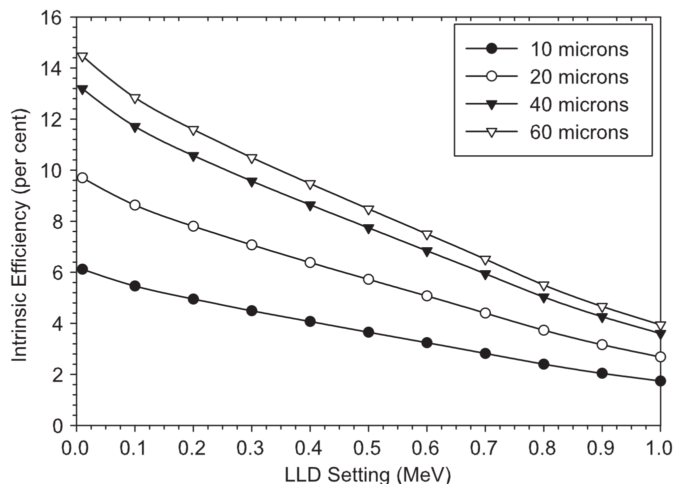

Fig. 7. Comparison of intrinsic efficiencies for different perforation depths for the cylindrical hole design. The unit cell width is 12 μm with 6-μm-diameter holes backfilled with ^{10}B.

Last is the case for unit cells 12 μm wide and with 6-μm-diameter holes (see Fig. 7). Here it is found that the hole diameter is approximately the same as the combined ranges of the reaction products [6]. As a result, the energy self-absorption problem increases, and the spectrum from the device will have an even higher response in the lower energy channels than for the previous two cases, resulting in an even larger fraction of the counts being discarded as the LLD is increased. This effect is quite noticeable in Fig. 7, in which the device with 10-μm-deep holes decreases from 6.1% ε_{tn} with the LLD = 0 to 3.2% ε_{tn} with the LLD = 600 keV. One concludes from these results that the smaller cell dimensions offer higher efficiencies with less dependence on the LLD setting. However, there is a practical limit to how small perforations can be made because of particle and electron trajectories considerations as well as fabrication limitations, issues to be addressed in a later section.

The estimated efficiencies of these devices are shown in Table 1, in which the LLD is set at 300 keV for all cases. From Table 1 it can be seen that there is a general trend for efficiency to increase as the ratio of the hole diameter to cell dimension (D/W_{cell}) increases. However, for small cell dimensions (⩽6 μm) at some point the amount of semiconductor mass diminishes to such small values that the energy deposited in the thin semiconductor regions is relatively small so that many pulses fall below 300 keV and the efficiency begins to decrease (compare D/W_{cell} values at 0.80 to those at 0.90). These same results indicate that there is a optimum cell width and feature size for each value of the LLD setting. From Table 1, one might conclude that the 4 μm cell with a $D/W_{cell} = 0.80$ is approaching the best design for all perforation depths. In this case the detector would have 3.2 μm-diameter holes with 0.8 μm thick walls between the holes at the narrowest points. The processing of such features can be challenging when trying to control oxidation and dopant diffusion, surface roughness, and other processing steps needed for detector fabrication. Some of these issues are addressed in a later section.

Table 1
Efficiencies for holes of diameter D and depth H filled with ^{10}B in a unit cell of width W_{cell}.

D/W_{cell}	Cell width W_{cell} (μm)				
	4	6	8	10	12
			Hole depth $H = 10$ μm		
0.10	0.31	0.31	0.31	0.30	0.30
0.20	1.22	1.20	1.18	1.16	1.13
0.30	2.71	2.63	2.55	2.45	2.33
0.40	4.73	4.53	4.29	3.96	3.44
0.50	7.24	6.81	6.19	5.20	4.49
0.60	10.20	9.33	7.73	6.47	5.58
0.70	13.54	11.73	9.30	7.79	6.72
0.80	16.49	13.73	10.92	9.12	7.88
0.90	16.32	13.62	12.05	10.44	9.07
			Hole depth $H = 20$ μm		
0.10	0.50	0.49	0.49	0.49	0.49
0.20	1.97	1.94	1.91	1.88	1.84
0.30	4.37	4.26	4.14	3.98	3.77
0.40	7.65	7.35	6.95	6.38	5.48
0.50	11.74	11.04	9.97	8.27	7.06
0.60	16.54	15.08	12.34	10.17	8.65
0.70	21.95	18.85	14.70	12.11	10.28
0.80	26.68	21.90	17.10	14.01	11.90
0.90	25.89	21.32	18.62	15.86	13.52
			Hole depth $H = 40$ μm		
0.10	0.68	0.68	0.67	0.67	0.67
0.20	2.69	2.66	2.62	2.58	2.52
0.30	5.99	5.85	5.68	5.46	5.17
0.40	10.49	10.10	9.54	8.73	7.47
0.50	16.11	15.16	13.64	11.27	9.57
0.60	22.72	20.68	16.81	13.78	11.64
0.70	30.14	25.79	19.95	16.31	13.74
0.80	36.61	29.86	23.11	18.78	15.81
0.90	35.22	28.80	25.02	21.15	17.86
			Hole depth $H = 60$ μm		
0.10	0.75	0.74	0.74	0.74	0.73
0.20	2.96	2.93	2.89	2.84	2.78
0.30	6.59	6.44	6.25	6.00	5.68
0.40	11.54	11.11	10.50	9.60	8.20
0.50	17.72	16.67	15.00	12.37	10.49
0.60	24.98	22.73	18.46	15.11	12.74
0.70	33.15	28.33	21.88	17.86	15.02
0.80	40.25	32.78	25.32	20.54	17.24
0.90	38.64	31.55	27.37	23.09	19.45

Neutrons are incident normally on the detector surface, and the LLD cutoff energy is 300 keV.

3.1.2. *Efficiencies for* ^{6}LiF *filled holes*

The combined range of ^{6}Li(n, t)^{4}He reaction products in both ^{6}LiF and Si is approximately 6 times that expected for ^{10}B(n, α)^{7}Li reaction products in ^{10}B and Si, thereby permitting the etched

feature sizes to be considerably larger. However, the macroscopic cross section for 2200 m/s neutrons is 57.5 cm^{-1}, a value considerably smaller than that of ^{10}B at 500.5 cm^{-1}. This smaller cross section requires that the perforations must be etched much deeper to achieve the same efficiency. Perhaps the single most important advantage of using ^{6}LiF as the converter material over ^{10}B is that the higher reaction product energies emitted from the ^{6}Li(n, t)^{4}He reaction are easier to distinguish from background gamma rays and, consequently, allow the LLD to be set much higher. The unit cells investigated here are 25, 50, and 75 μm wide, and the perforation depths are 90, 175, 350 and 500 μm. The holes are assumed to be backfilled with ^{6}LiF. Again the semiconductor used for the calculations was silicon.

In Fig. 8 the estimated efficiencies are shown as a function of the LLD setting for the cases in which the unit cell is 25 μm wide and the holes are 12.5 μm in diameter (50% of the unit cell dimension). The zero LLD condition produces the highest possible efficiencies ε_{tn}, ranging from 7.7% for 90-μm-deep holes to 18.2% for 500-μm-deep holes. The design produces a fairly consistent or constant response to thermal neutrons for LLD settings up to 800 keV, dropping to only 7.4% for 90-μm-deep holes and to only 17.7% for 500-μm-deep holes. This property is important because an LLD of 300 keV or more is often needed for discrimination of gamma-ray background.

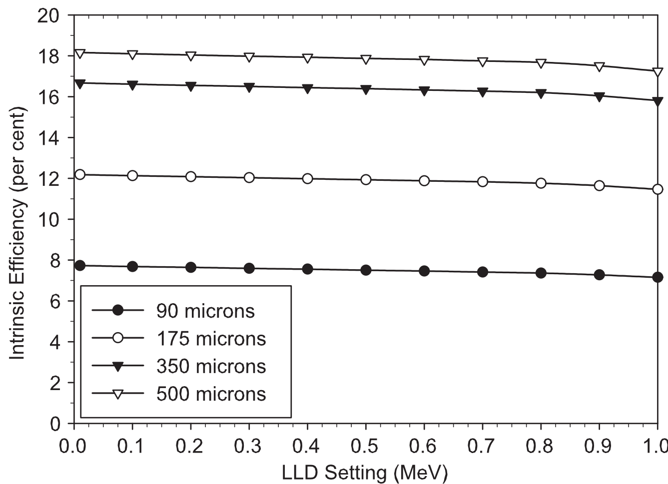

Fig. 8. Comparison of intrinsic efficiencies for different perforation depths for the cylindrical hole design. The unit cell width is 25 μm with 12.5 μm-diameter holes backfilled with ^{6}LiF.

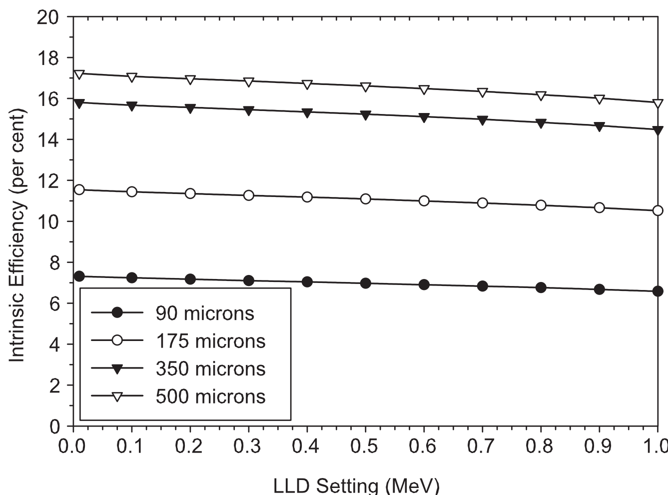

Fig. 9. Comparison of intrinsic efficiencies for different perforation depths for the cylindrical hole design. The unit cell width is 50 μm with 25 μm-diameter holes backfilled with ^{6}LiF.

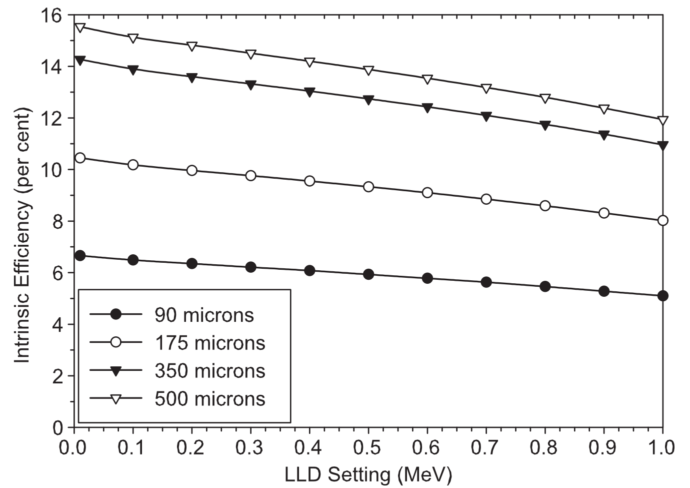

Fig. 10. Comparison of intrinsic efficiencies for different perforation depths for the cylindrical hole design. The unit cell width is 75 μm with 37.5 μm-diameter holes.

Shown in Fig. 9 are the calculated efficiencies as a function of the LLD setting for the cases in which the unit cell is 50 μm wide and the holes are 25 μm in diameter (again 50% of the unit cell dimension). The ε_{tn} for a LLD setting of 0 ranges from 7.3% for 90-μm-deep holes to 17.2% for 500-μm-deep holes.

Finally, results for the cases in which the unit cells are 75 μm wide with 37.5-μm-diameter holes are shown in Fig. 10. In these cases the hole diameter is approximately the same as the combined ranges of the reaction products [6], and it is seen the efficiencies noticeably decrease as the LLD setting is increased. This decrease results from greatly increased energy self-absorption in the ^{6}LiF before the ions enter the semiconductor. As a consequence, the energy-deposition spectrum from the device has more counts in the lower energy channels than for the previous cases and, hence, a larger percentage of counts is discarded as the LLD is increased.

The calculated efficiencies of these devices for an LLD of 300 keV are shown in Table 2. From this table it is seen that there is a general trend for efficiency to increase as the ratio of the hole diameter to cell dimension (D/W_{cell}) increases. There is most likely an optimum cell width and feature size for each value of the LLD setting although is not evident from the results of Table 2. For instance, a cell width of 20 μm with a D/W_{cell} ratio of 0.90 has a 18-μm-diameter hole with a minimum semiconductor thickness of 2 μm at the narrowest points between the holes. As a result, there is still enough energy deposited in the semiconductor such that a significant fraction of events deposit more than 300 keV. Should the D/W_{cell} ratio be increased, the energy deposition would eventually fall below 300 keV, and the efficiency would decrease. As before, the fabrication of such small features can be challenging and perhaps not practicable.

3.2. *Straight trench-shaped perforations*

Another structure investigated as a perforated detector is one with trench-shaped perforations etched into the semiconductor [7,15,16]. This design offers a high probability of capturing ion reaction products, provided that the trench width is less than the sum of the ranges of both reaction ions. In Fig. 11 are shown the possible trajectories that reaction ions from either the ^{10}B(n, α)^{7}Li or ^{6}Li(n, t)^{4}He reactions can follow. In trajectory (1), ions are

Table 2
Efficiencies for holes of diameter D and depth H filled with ^{6}LiF in a unit cell of width W_{cell}.

D/W_{cell}	Cell width w_{cell} (μm)				
	20	40	60	80	100
	Hole depth $H = 90\,\mu$m				
0.10	0.32	0.32	0.31	0.31	0.31
0.20	1.26	1.24	1.22	1.20	1.17
0.30	2.81	2.74	2.66	2.57	2.46
0.40	4.96	4.78	4.58	4.29	3.81
0.50	7.68	7.32	6.84	5.96	5.07
0.60	10.95	10.30	9.18	7.53	6.34
0.70	14.78	13.63	11.30	9.11	7.64
0.80	18.95	17.17	13.38	10.69	8.97
0.90	22.01	19.14	15.46	12.35	10.38
	Hole depth $H = 175\,\mu$m				
0.10	0.50	0.50	0.49	0.49	0.49
0.20	1.98	1.96	1.93	1.90	1.86
0.30	4.43	4.34	4.23	4.08	3.89
0.40	7.83	7.59	7.26	6.78	5.97
0.50	12.15	11.62	10.82	9.33	7.85
0.60	17.35	16.34	14.43	11.68	9.69
0.70	23.43	21.58	17.65	13.99	11.52
0.80	30.09	27.11	20.75	16.26	13.38
0.90	34.79	30.01	23.79	18.58	15.28
	Hole depth $H = 350\,\mu$m				
0.10	0.68	0.68	0.67	0.67	0.67
0.20	2.71	2.68	2.64	2.60	2.55
0.30	6.07	5.95	5.80	5.60	5.34
0.40	10.72	10.41	9.96	9.28	8.14
0.50	16.65	15.94	14.83	12.73	10.64
0.60	23.80	22.41	19.73	15.86	13.06
0.70	32.14	29.59	24.04	18.90	15.43
0.80	41.31	37.12	28.17	21.86	17.82
0.90	47.66	40.96	32.18	24.86	20.21
	Hole depth $H = 500\,\mu$m				
0.10	0.74	0.74	0.73	0.73	0.73
0.20	2.95	2.92	2.88	2.84	2.78
0.30	6.61	6.49	6.33	6.11	5.82
0.40	11.68	11.35	10.86	10.11	8.86
0.50	18.14	17.39	16.16	13.86	11.57
0.60	25.94	24.44	21.49	17.25	14.18
0.70	35.04	32.25	26.17	20.54	16.74
0.80	45.05	40.46	30.64	23.73	19.29
0.90	51.94	44.61	34.97	26.95	21.85

Neutrons are incident normally on the detector surface, and the LLD cutoff energy is 300 keV.

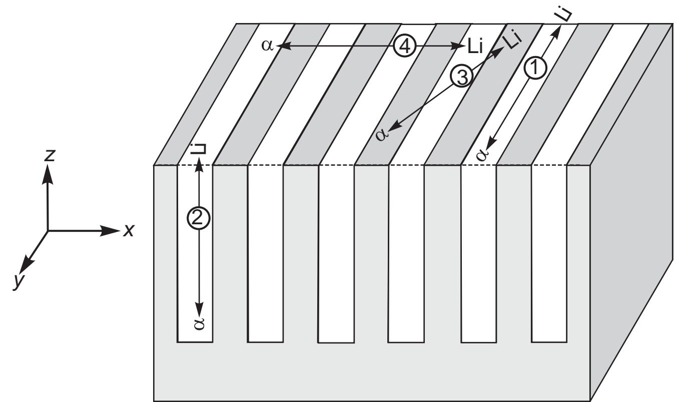

Fig. 11. There are many trajectories for reaction products in a perforated trench design. The main trajectories of interest are shown here, where (1) a complete miss occurs if the reaction products travel in the y direction, (2) a complete miss occurs if the reaction products travel in the z direction, (3) one or both charged particles are absorbed in the semiconductor, and (4) with small dimensions, one or more charged particle reaction products can traverse another absorber (^{10}B, ^{6}LiF) trench, which reduces the energy absorbed in the semiconductor.

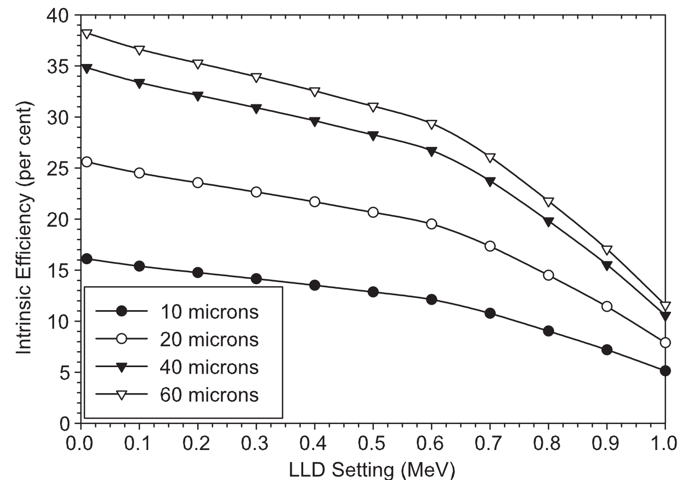

Fig. 12. Comparison of intrinsic efficiencies as a function of perforation depth for the straight trench design. The unit cell is 4 μm wide and the 2-μm-wide trenches are backfilled with ^{10}B.

emitted parallel to the perforation axis (y direction) and do not enter into the semiconductor; hence, they would not be recorded. Also in trajectory (2), the particles are emitted longitudinally along the perforation (z direction) and do not enter into the semiconductor, hence again would not be recorded. However, trajectories (3) and (4), and their variants, would in fact result in one or both particles entering the semiconductor and possible produce a count. Should an event occur in which the distance between trenches is smaller than an ion range, then the ion may enter the adjacent trenches and deposit less energy in the semiconductor, as depicted in trajectory (4). The probability of these various trajectories and resultant energy deposition are a function of the fill material, trench width and pitch.

3.2.1. *Efficiencies of* ^{10}B *filled trenches*

Considered here are unit cells with widths of 4, 8, and 12 μm and with trench depths of 10, 20, 40 and 60 μm to be consistent with the analyses of the hole perforations. In the present case, the holes were backfilled with ^{10}B with a 2200-m/s macroscopic cross section of 500.5 cm^{-1}. The semiconductor is silicon with a mass density of 2.33 g/cm^{3} and Z of 14.

Shown in Fig. 12 are the calculated efficiencies as a function of the LLD setting for the cases in which the unit cell is 4 μm wide and the trenches are 2 μm wide (50% of the unit cell dimension). The zero LLD condition is the highest possible efficiency, ranging from 16.1% for 10-μm-deep trenches to 38.2% for 60-μm-deep trenches. The design yields a fairly slow decrease in efficiency as the LLD varies from 0 to 600 keV, dropping from 16.1% to 12.1% for 10-μm-deep trenches and from 38.2% to 29.4% for 60-μm-deep trenches. Here it is seen that the trench design can achieve higher efficiencies than the hole design, yet is more sensitive to changes in the LLD setting.

In Fig. 13 calculated efficiencies are shown as a function of the LLD setting for the cases of 8 μm wide cells with trenches 4 μm wide. With the LLD set to 0 keV, ε_{tn} varies from 12.8% for 10-μm-deep trenches up to 29.2% for 60-μm-deep trenches. The efficiencies noticeably decrease as the LLD is increased, a consequence of energy self-absorption in the trenches before the reaction ions enter the semiconductor. As a result, the energy-deposition spectra from

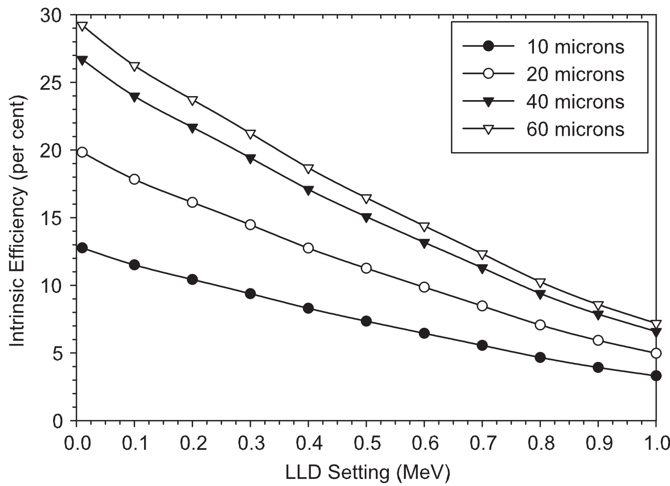

Fig. 13. Comparison of intrinsic efficiencies for different perforation depths for the straight trench design. The unit cell is 8 μm wide and the 4-μm-wide trenches are backfilled with ^{10}B.

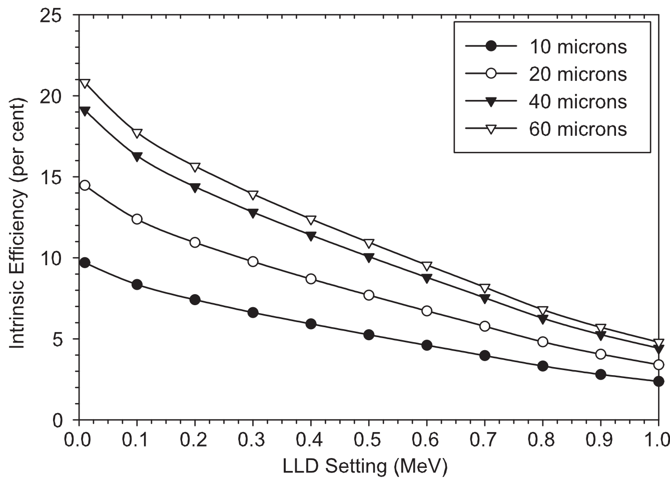

Fig. 14. Comparison of intrinsic efficiencies for different perforation depths for the straight trench design. The unit cell is 12 μm wide and the 6-μm-wide trenches are backfilled with ^{10}B.

these devices have more counts in the lower energy channels than for the previous cases and, consequently more counts are discarded as the LLD is increased.

Finally are the cases in which the unit cells are 12 μm with 6-μm-wide trenches (Fig. 14). In these cases the trench width is approximately the same as the combined ranges of the reaction products [6]. As a result, the energy self-absorption problem in the trenches increases, and the energy-deposition spectra from these devices have an even higher number of counts in the lower energy channels than those for the previous cases. Thus, a larger percentage of counts are discarded as the LLD is increased, resulting in decreased efficiencies and larger fractional changes in the efficiencies as the LLD is increased.

The calculated efficiencies of these devices for an LLD setting of 300 keV are given in Table 3. From Table 3 it can be seen that there is a general trend for efficiency to increase as the ratio of the trench width to cell dimension (T/W_{cell}) increases. However, for small cell T/W_{cell} ratios the amount of semiconductor mass diminishes to such small values that the energy deposited in the thin semiconductor regions is relatively small, hence a significant number of pulses fall below 300 keV and the efficiency begins to decrease (compare T/W_{cell} values above and below ≈ 0.70). These same results indicate that there is a optimum cell width and feature size for each LLD setting. From Table 3, one might conclude that the 4-μm-wide cell with a $D/W_{cell} = 0.70$ approaches the optimum design for most perforation depths. For a 4-μm-wide cell, the detector would have 2.8-μm-diameter holes with 1.2-μm-thick walls between the holes at that narrowest points. Although processing of such features is feasible, oxidation and dopant diffusion, surface roughness, and other processing steps can seriously diminish the sensitive silicon volume, hence reducing the actual device efficiency from that estimated here.

Table 3
Efficiencies for straight trenches of width T and depth H filled with ^{10}B in a unit cell of width W_{cell}.

T/W_{cell}	Cell width W_{cell} (μm)				
	4	6	8	10	12
			Trench depth $H = 10$ μm		
0.10	3.70	3.58	3.47	3.35	3.24
0.20	6.94	6.49	6.07	5.66	5.26
0.30	9.73	8.79	7.90	7.04	6.19
0.40	12.13	10.53	9.01	7.49	6.36
0.50	14.17	11.74	9.38	7.67	6.62
0.60	15.80	12.40	9.53	7.94	6.90
0.70	17.09	12.44	9.79	8.24	7.17
0.80	15.51	12.66	10.06	8.49	7.45
0.90	6.10	7.43	8.40	8.55	7.71
			Trench depth $H = 20$ μm		
0.10	5.95	5.76	5.58	5.40	5.22
0.20	11.16	10.44	9.74	9.06	8.38
0.30	15.65	14.10	12.58	11.11	9.64
0.40	19.48	16.78	14.16	11.56	9.61
0.50	22.67	18.52	14.46	11.55	9.75
0.60	25.16	19.31	14.41	11.70	9.93
0.70	27.06	19.14	14.54	11.88	10.08
0.80	24.11	19.07	14.70	12.01	10.24
0.90	7.46	9.88	11.60	11.81	10.37
			Trench depth $H = 40$ μm		
0.10	8.14	7.89	7.63	7.38	7.14
0.20	15.27	14.28	13.32	12.36	11.41
0.30	21.41	19.26	17.14	15.07	13.00
0.40	26.63	22.86	19.17	15.52	12.78
0.50	30.94	25.13	19.41	15.33	12.81
0.60	34.28	26.06	19.16	15.36	12.88
0.70	36.75	25.54	19.16	15.44	12.90
0.80	32.48	25.45	19.22	15.45	12.96
0.90	8.78	12.27	14.72	14.99	12.97
			Trench depth $H = 60$ μm		
0.10	8.95	8.67	8.39	8.11	7.85
0.20	16.78	15.69	14.63	13.58	12.53
0.30	23.53	21.16	18.81	16.53	14.23
0.40	29.26	25.10	21.01	16.98	13.95
0.50	33.99	27.55	21.23	16.71	13.93
0.60	37.63	28.53	20.91	16.70	13.96
0.70	40.31	27.91	20.87	16.75	13.94
0.80	35.55	27.77	20.88	16.71	13.96
0.90	9.26	13.14	15.86	16.17	13.91

Neutrons are incident normally on the detector surface, and the LLD cutoff energy is 300 keV.

3.2.2. *Efficiencies of* ^{6}LiF *filled trenches*

The unit cell widths investigated are 25, 50, and 75 μm and the depths are 90, 175, 350 and 500 μm to be consistent with the earlier perforated hole analyses. In the present case, the trenches

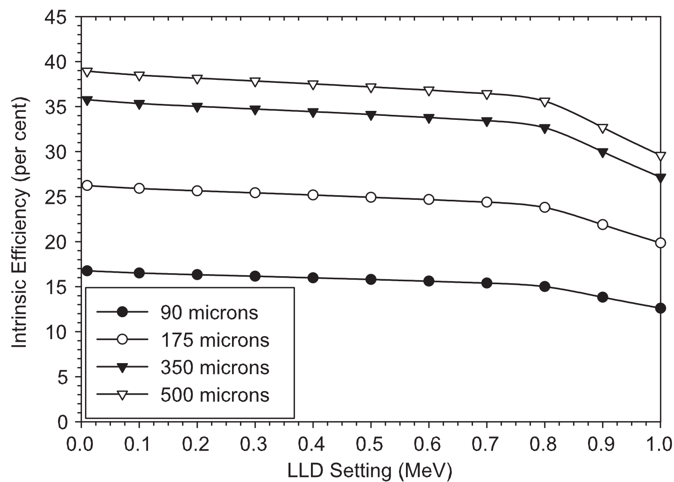

Fig. 15. Comparison of intrinsic efficiencies for different perforation depths for the straight trench design. The unit cell dimensions are 25 μm with 12.5 micron wide trenches, and the perforations are backfilled with ^{6}LiF.

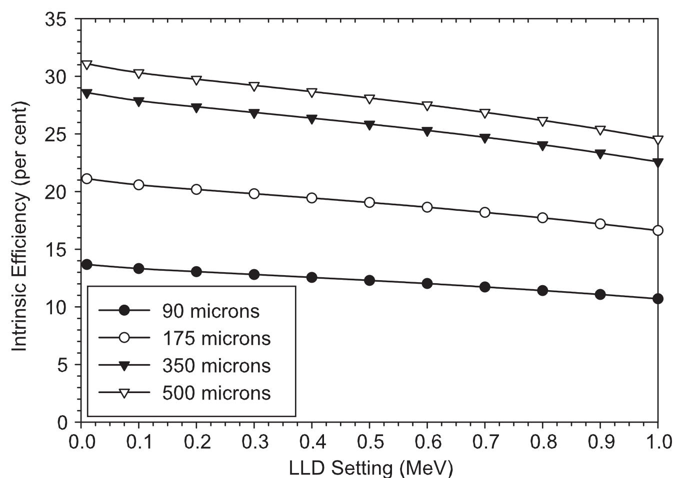

Fig. 16. Comparison of intrinsic efficiencies for different perforation depths for the straight trench design. The unit cell dimensions are 50 μm with 25 micron wide trenches and the perforations are backfilled with ^{6}LiF.

are backfilled with ^{6}LiF. The semiconductor used for the calculations is again Si.

In Fig. 15 are shown the computed efficiencies as a function of the LLD setting for cases in which the unit cell is 25 μm wide and the trenches are 12.5 μm wide (50% of the unit cell dimension). The zero LLD setting has the highest possible efficiency, ranging from 16.8% intrinsic thermal-neutron detection efficiency for 90-μm-deep holes to 38.9% for 500-μm-deep holes. This design has a slowly decreasing efficiency as the LLD setting varies from 0 to 800 keV, dropping from 16.8% to 15.0% for 90-μm-deep trenches, and from 38.9% to 35.6% for 500-μm-deep trenches. Here it is seen that the trench design can achieve higher efficiencies than the hole design, while being slightly more sensitive to changes in the LLD setting.

In Fig. 16 the computed efficiencies are shown as a function of the LLD setting for the cases in which the unit cell is 50 μm wide and the trenches are 25 μm wide. With the LLD set to 0 keV, ε_{tn} ranges from 13.7% for 90-μm-deep trenches to 31.1% for 500-μm-deep trenches. The efficiencies noticeably decrease as the LLD is increased, a consequence of energy self-absorption in the ^{6}LiF before the reaction ions enter the semiconductor. As a result, the energy-deposition spectrum from this detector has more counts

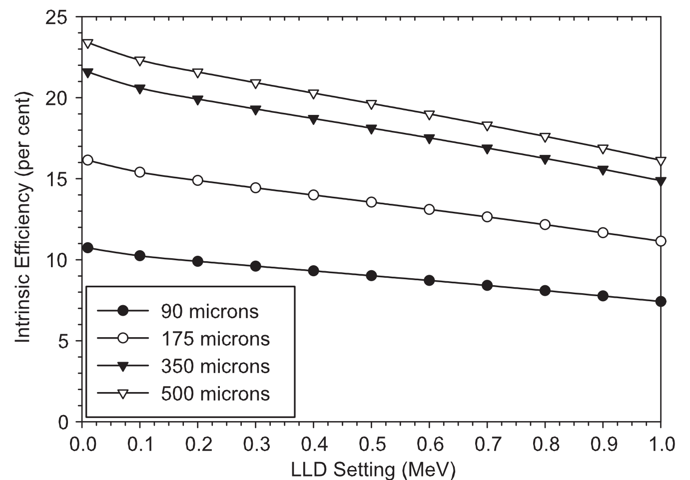

Fig. 17. Comparison of intrinsic efficiencies for different perforation depths for the straight trench design. The unit cell dimensions are 75 μm with 37.5 micron wide trenches, and the perforations are backfilled with ^{6}LiF.

in the lower energy channels than those from the smaller 25-μm unit-cell detector, and, consequently, a larger number of counts are discarded as the LLD setting is increased.

Finally, results for a detector with a 75-μm unit cell and 37.5-μm-wide trenches are shown in Fig. 17. In these cases the trench width is approximately the same as the combined ranges of the reaction products. As a result, the energy self-absorption problem increases, and the spectrum from the device will have an even higher number of counts in the lower energy channels than the previous case, resulting in a larger percentage being discarded as the LLD is increased. This effect results in decreased efficiencies and larger fractional changes in the efficiency as the LLD is increased.

The calculated efficiencies of trenched devices are given in Table 4, in which the LLD was set at 300 keV for all cases. From Table 4 it can be seen that there is again a general trend for efficiency to increase as the ratio of the trench width to cell dimension (T/W_{cell}) increases. However, for small cell T/W_{cell} ratios the amount of semiconductor mass diminishes to such small values that the energy deposited in the thin semiconductor regions is relatively small; hence, a significant number of pulses fall below 300 keV and the efficiency begins to decrease (compare T/W_{cell} values above and below ≈ 0.80). These same results indicate that there is a optimum cell width and feature size for each value of the LLD setting.

3.3. Pillar devices

To fabricate a pillar device a large perforation is etched into the semiconductor to form a square matrix of miniature cylindrical columns. The space around the columns is then backfilled with a neutron reactive material. The authors of citations [8,17] claim that a Si device with 2-μm-diameter pillars with a center to center pitch of 4 μm has an efficiency greater than 65% for 50-μm-high pillars surrounded by enriched ^{10}B. In this geometry, 80.3% of the surface is covered by ^{10}B and 91.8% of the thermal neutrons normally incident on the 50-μm-thick ^{10}B surface will be absorbed. Hence, only 73.77% of neutrons normally incident on the surface of such a device are absorbed. The claim of 65% thermal-neutron detection efficiency would indicate that over 88% of the reactions produce a count, a result which seems incorrect in light of the analyses on hole and trench structures presented here and elsewhere [7]. Smaller dimensions, 0.2-μm cell dimensions and 0.1-μm-diameter pillars, each 50 μm deep,

Table 4
Efficiencies for straight trenches of width T and depth H filled with ^{6}LiF in a unit cell of width W_{cell}.

T/W_{cell}	Cell width W_{cell} (μm)				
	20	40	60	80	100
	Trench depth $H = 90\,\mu m$				
0.10	3.90	3.75	3.62	3.49	3.37
0.20	7.51	6.98	6.52	6.08	5.65
0.30	10.85	9.78	8.79	7.83	6.90
0.40	13.97	12.15	10.45	8.78	7.27
0.50	16.87	14.12	11.49	9.11	7.58
0.60	19.55	15.68	11.93	9.38	7.87
0.70	22.04	16.84	12.23	9.69	8.19
0.80	22.23	17.56	12.51	9.97	8.49
0.90	14.42	13.57	12.65	10.31	8.80
	Trench depth $H = 175\,\mu m$				
0.10	6.13	5.91	5.71	5.51	5.32
0.20	11.83	11.01	10.25	9.53	8.81
0.30	17.11	15.39	13.75	12.14	10.56
0.40	22.03	19.05	16.20	13.38	10.86
0.50	26.58	22.03	17.60	13.61	11.05
0.60	30.76	24.32	18.00	13.74	11.22
0.70	34.63	25.91	18.18	13.95	11.41
0.80	34.77	26.76	18.33	14.10	11.61
0.90	21.25	19.91	18.25	14.33	11.79
	Trench depth $H = 350\,\mu m$				
0.10	8.37	8.08	7.81	7.53	7.27
0.20	16.17	15.07	14.02	13.00	11.99
0.30	23.42	21.04	18.74	16.48	14.25
0.40	30.14	26.00	21.99	18.02	14.48
0.50	36.35	29.99	23.75	18.14	14.54
0.60	42.05	33.01	24.11	18.13	14.59
0.70	47.30	35.04	24.17	18.22	14.66
0.80	47.40	36.02	24.19	18.26	14.75
0.90	28.13	26.29	23.89	18.36	14.80
	Trench depth $H = 500\,\mu m$				
0.10	9.12	8.81	8.51	8.21	7.92
0.20	17.62	16.42	15.27	14.16	13.05
0.30	25.52	22.92	20.40	17.92	15.48
0.40	32.84	28.31	23.92	19.56	15.69
0.50	39.61	32.64	25.80	19.65	15.71
0.60	45.81	35.90	26.14	19.60	15.71
0.70	51.52	38.08	26.16	19.64	15.75
0.80	51.61	39.11	26.15	19.64	15.79
0.90	30.42	28.42	25.76	19.70	15.80

Neutrons are incident normally on the detector surface, and the LLD cutoff energy is 300 keV.

are claimed to produce thermal-neutron detection efficiencies reaching 85% [17], a puzzling claim because, with the geometry described, only 73.77% of neutrons normally incident on the device would be absorbed using ^{10}B as the absorber.

3.3.1. *Efficiencies of pillars surrounded by* ^{10}B

The unit cell for the pillar design is depicted in Fig. 3. Again three unit-cell structures and four different pillar heights are investigated. The unit cells are 4, 8, and 12 μm wide, and the pillars are 10, 20, 40 and 60 μm tall. In these cases, the silicon pillars are surrounded by ^{10}B.

In Fig. 19 the calculated efficiencies are shown as a function of the LLD setting for the cases in which the unit cell is 4 μm in size and the pillars are 2 μm in diameter (50% of the unit cell dimension). The zero LLD setting produces the highest possible efficiencies, ranging from 18.1% intrinsic thermal-neutron detection efficiency for 10-μm-tall pillars to 40.2% for 60-μm-tall pillars. The efficiency for the pillar design is strongly dependent

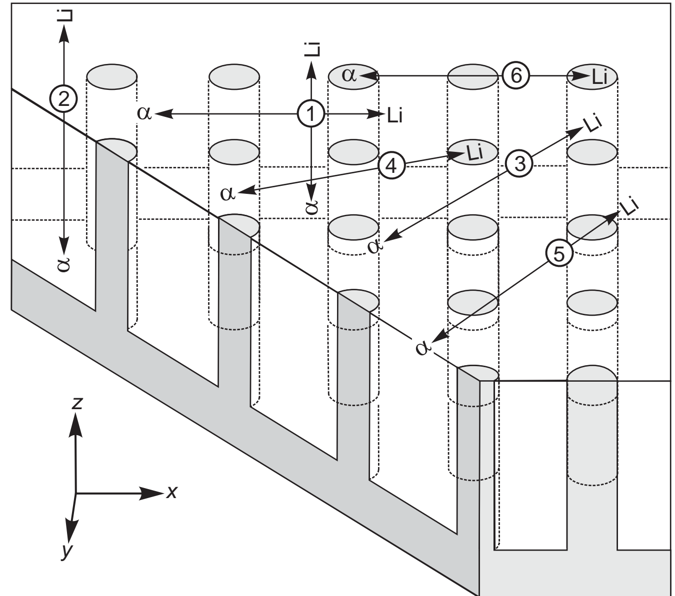

Fig. 18. There are many more different trajectories for reaction products in a pillar structure than for the hole and trench structures. The main trajectories of interest are shown here, where (1) a complete miss can occur if the reaction products travel along the x or y directions, (2) a complete miss occurs if the reaction products travel in the z direction, (3) a miss occurs if the reaction products travel in certain critical angles to the Si columns, (4) only one charged particle reaches the semiconductor, (5) both charged particles reach the semiconductor, and (6) with small dimensions, one or more charged particle reaction products can traverse more than one Si pillar, which increases the energy absorption in the semiconductor.

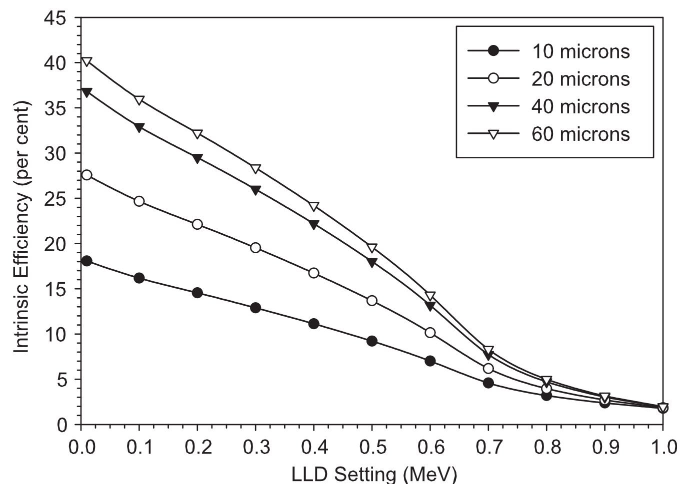

Fig. 19. Comparison of intrinsic efficiencies as a function of pillar height for the pillar design. The unit cell dimensions are 4 μm and the reactive material surrounding the pillars is ^{10}B. Pillar diameters are 2 microns.

upon the LLD setting, decreasing rapidly as the LLD setting increases. At an LLD setting of 500 keV, the efficiency drops to 9.2% for 10-μm pillars and to 19.6% for 60-μm pillars. This rapid decrease is a direct consequence of the design. The pillars are too small to absorb all of the energy from the reaction ions, as shown by trajectories (5) and (6) in Fig. 18, which leads to ion energy depositions that accumulate in the low-energy portion of the pulse height spectrum. As a result, a significant fraction of counts is eliminated for each increasing increment of the LLD setting. Unfortunately, in the presence of a gamma-ray field, which generally accompanies a neutron emitter, the high efficiency of

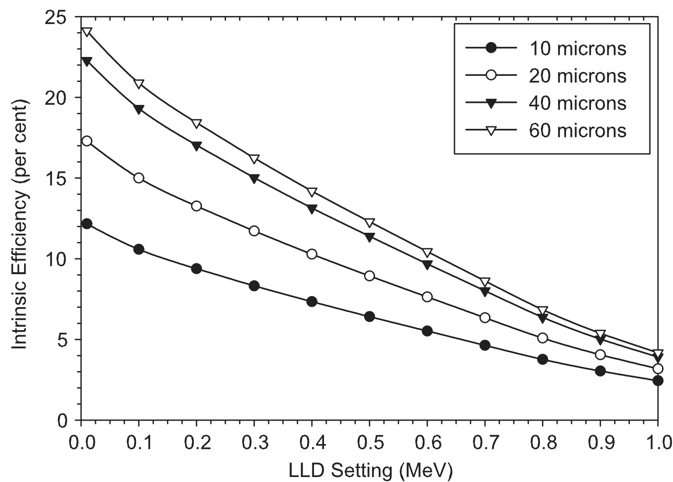

Fig. 20. Comparison of intrinsic efficiencies as a function of pillar height for the pillar design. The unit cell dimensions are 8 μm and the reactive material surrounding the pillars is ^{10}B. Pillar diameters are 4 microns.

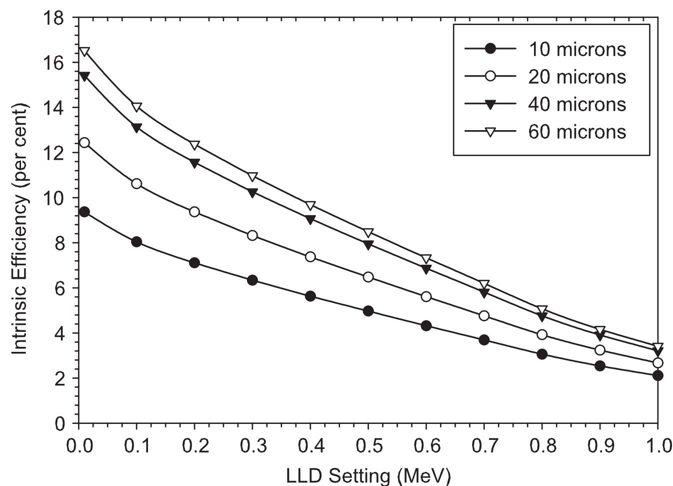

Fig. 21. Comparison of intrinsic efficiencies as a function of pillar height for the pillar design. The unit cell dimensions are 12 μm and the reactive material surrounding the pillars is ^{10}B. Pillar diameters are 6 microns.

Table 5
Efficiencies for cylindrical silicon pillars of diameter D and height H surrounded by ^{10}B in a unit cell of width W_{cell}.

D/W_{cell}	Cell width W_{cell} (μm)				
	4	6	8	10	12
			Pillar height $H = 10$ μm		
0.10	2.91	3.02	3.14	3.34	3.40
0.20	4.23	5.13	4.85	4.53	4.28
0.30	8.01	7.01	6.10	5.47	5.03
0.40	10.76	8.74	7.26	6.32	5.72
0.50	12.89	10.17	8.32	7.13	6.34
0.60	14.36	11.29	9.37	7.91	6.91
0.70	14.91	11.91	10.00	8.60	7.49
0.80	14.24	11.86	10.01	8.77	7.78
0.90	11.94	10.64	9.04	7.96	7.19
			Pillar height $H = 20$ μm		
0.10	1.83	2.03	2.29	2.62	2.72
0.20	4.19	5.74	5.28	4.72	4.30
0.30	10.79	9.11	7.52	6.44	5.67
0.40	15.67	12.20	9.67	8.08	7.05
0.50	19.53	14.86	11.70	9.69	8.31
0.60	22.29	17.06	13.78	11.27	9.57
0.70	23.56	18.43	15.18	12.78	10.87
0.80	22.76	18.71	15.58	13.43	11.75
0.90	19.23	17.03	14.30	12.47	11.14
			Pillar height $H = 40$ μm		
0.10	0.79	1.08	1.44	1.92	2.05
0.20	4.16	6.33	5.70	4.91	4.31
0.30	13.51	11.14	8.91	7.40	6.31
0.40	20.44	15.55	12.02	9.80	8.33
0.50	26.00	19.45	15.01	12.18	10.23
0.60	30.03	22.68	18.07	14.55	12.16
0.70	31.98	24.79	20.21	16.85	14.17
0.80	31.07	25.38	20.97	17.98	15.62
0.90	26.33	23.25	19.40	16.85	14.99
			Pillar height $H = 60$ μm		
0.10	0.41	0.73	1.13	1.66	1.81
0.20	4.15	6.55	5.85	4.99	4.32
0.30	14.51	11.88	9.43	7.74	6.54
0.40	22.19	16.79	12.87	10.43	8.81
0.50	28.38	21.14	16.23	13.10	10.94
0.60	32.87	24.75	19.65	15.75	13.12
0.70	35.07	27.13	22.07	18.34	15.38
0.80	34.12	27.83	22.96	19.65	17.04
0.90	28.94	25.53	21.29	18.46	16.41

Neutrons are incident normally on the detector surface, and the LLD cutoff energy is 300 keV.

the pillar design is compromised as the LLD is set high enough to eliminate the gamma-ray background. Further, the use of this device would require the operator to understand the drastic changes in the detector efficiency as a function of the LLD setting, a deficiency not shared by the hole or trench designs with similar cell dimensions. This rapid variation of efficiency with the LLD setting is a major deficiency of the pillar design (Fig. 19).

In Fig. 20 results are presented for the cases in which the unit cell is 8 μm wide and the pillars are 4 μm in diameter (again 50% of the unit cell dimension). The ε_{tn} values range from 12.2% for 10-μm-tall pillars up to 24.1% for 60-μm-tall pillars. Again the efficiencies rapidly decrease as the LLD is increased as a consequence of inefficient energy deposition in the pillar and energy self-absorption in the ^{10}B before the reaction ions reach the Si pillars. As a result, the energy deposition spectrum from this device is confined mostly to the lower energy channels, and as the LLD setting is increased the efficiency decreases rapidly.

Results for 12-μm unit cells with 6-μm-diameter pillars are shown in Fig. 21. In these cases the pillar diameter is larger than either reaction ions range, hence the ^{10}B can absorb the entire energy of either reaction ion. Only those reaction ions produced near the pillar surface can enter the pillar with almost their full energy. Also the geometry of the design allows only one ion to reach the Si so that only one of the reaction ions can be counted, a deficiency similar, in many ways, to the planar coated detector design [6]. Further, because the maximum range of the alpha particle emissions is approximately 4.2 μm in ^{10}B, there are zones in the ^{10}B region from which reaction particles can not reach the pillars. As a result, the energy self-absorption problem increases, and the spectrum from the device will have a high representation in the lower energy channels, resulting in a large percentage being discarded as the LLD is increased. This effect is quite noticeable in Fig. 21, in which the device with 10-μm pillars decreases from 9.4% with the LLD = 0, to 6.3% with the LLD = 300 keV, and down to 5.0% with the LLD = 500 keV. Thus, it is seen that a pillar design with small cell dimensions can offer high efficiencies; however, all of the pillar designs suffer from a strong dependence of the efficiency on the LLD setting.

The calculated efficiencies of some pillar devices are given in Table 5, in which the LLD is set at 300 keV for all cases. From Table 5 it can be seen that there is again a general trend for efficiency to

increase as the ratio of the pillar diameter to cell dimension (D/W_{cell}) increases. However, for small cell dimensions ($\leqslant$ 6 μm) at some point the amount of absorber material diminishes to such small values that the probability of absorbing a neutron becomes relatively small so that efficiency begins to decrease (compare D/W_{cell} values at 0.70 to those at 0.90). These same results indicate that there is a optimum cell width and feature size for each value of LLD setting. From Table 5, one might conclude that the 4-μm cell with a $D/W_{cell} = 0.70$ is approaching the best design for all perforation depths. In such a case the detector would have 2.8-μm-diameter pillars with 1.2-μm thick absorber regions between the pillars at the narrowest points.

3.3.2. *Efficiencies of pillars surrounded by* ^{6}LiF

The unit cells investigated here are 25, 50, and 75 μm with pillar heights of 90, 175, 350 and 500 μm. These dimensions are chosen to be consistent with the earlier analysis of hole and trench devices. Here the perforation surrounding the Si pillars is backfilled with ^{6}LiF.

In Fig. 22 the calculated efficiencies are shown as a function of the LLD setting for the 25-μm unit cells with pillars 12.5 μm in diameter (50% of the unit cell dimension). At an LLD setting of 0 keV, the highest possible efficiencies are realized, ranging from 19.4% for 90-μm-tall pillars to 43.2% for 500-μm-tall pillars. Again the efficiency decreases as the LLD setting is increased, yet not as severely as seen with the ^{10}B backfilled pillar design. At an LLD setting of 300 keV, the efficiency drops to 17.2% for 90-μm pillars to 38.2% for 500-μm pillars. For an LLD setting of 500 keV, the efficiency drops to 15.0% for 90-μm pillars and to 33.0% for 500-μm pillars. These devices suffer from the same deficiencies as the ^{10}B pillar devices.

Fig. 23 shows similar results for pillar devices with 50-μm unit cells and 25-μm pillars (again 50% of the unit cell dimension). The ε_{tn} values at LLD = 0 range from 12.9% for 90-μm pillars to 26.5% for 500-μm pillars. Again the efficiencies noticeably decrease as the LLD is increased as a consequence of partial energy absorption in the pillar and relatively large energy self-absorption in the ^{6}LiF material. The general trend is a decrease in efficiency as the unit cell dimensions are increased.

Finally, results for devices with 75-μm unit cells with 37.5-μm-diameter pillars are shown in Fig. 24. Now the pillar diameter is larger than either reaction product range and, hence, can absorb the entire energy of either reaction product. These dimensions permit only one reaction ion to deposit energy in the silicon pillar. Further, because the maximum range of the proton emissions is approximately 28 μm in ^{6}LiF and that of the alpha particle is 6 μm, there are dead zones in the reactive ^{6}LiF fill from which neither reaction ion can reach the pillars. As a result, the energy self-absorption problem increases, and the spectrum from the device will have a high representation in the lower energy channels, resulting in a large percentage being discarded as the LLD is increased. This effect is quite noticeable in Fig. 24, in which the device with 10-μm-deep holes decreases its efficiency from 9.8% with the LLD = 0, to 9% with the LLD = 300 keV, and down to 8.3% with the LLD = 500 keV. Again it is seen that the smaller cell dimensions offer higher efficiency. However, none of the pillar designs offers near constant efficiencies as a function of LLD.

The calculated efficiencies of these devices are listed in Table 6, in which the LLD = 300 keV for all cases. From Table 6 it can be seen that there is again a general trend for efficiency to increase as the ratio of the pillar diameter to cell dimension (D/W_{cell}) increases. As with the ^{10}B pillar devices, there is an optimum D/W_{cell} that produces the maximum efficiency for a given size of unit cell. From Table 6, one might conclude that the 20-μm cell

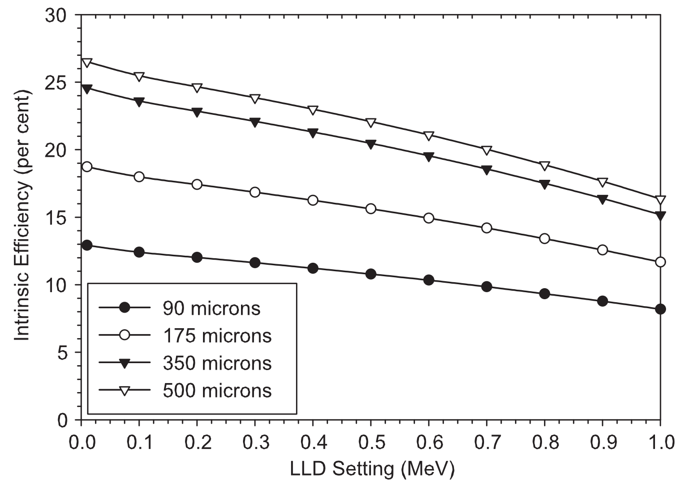

Fig. 23. Comparison of intrinsic efficiencies as a function of pillar height for the pillar design. The unit cell dimensions are 50 μm and the reactive material surrounding the pillars is ^{6}LiF. Pillar diameters are 25 microns.

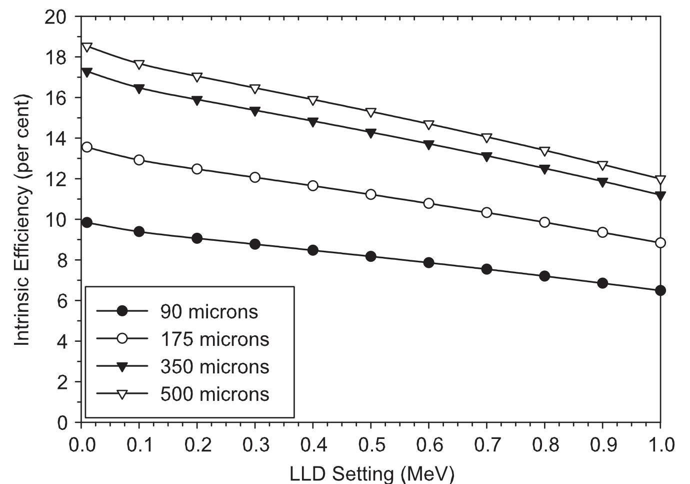

Fig. 24. Comparison of intrinsic efficiencies as a function of pillar height for the pillar design. The unit cell dimensions are 75 μm and the reactive material surrounding the pillars is ^{6}LiF. Pillar diameters are 37.5 microns.

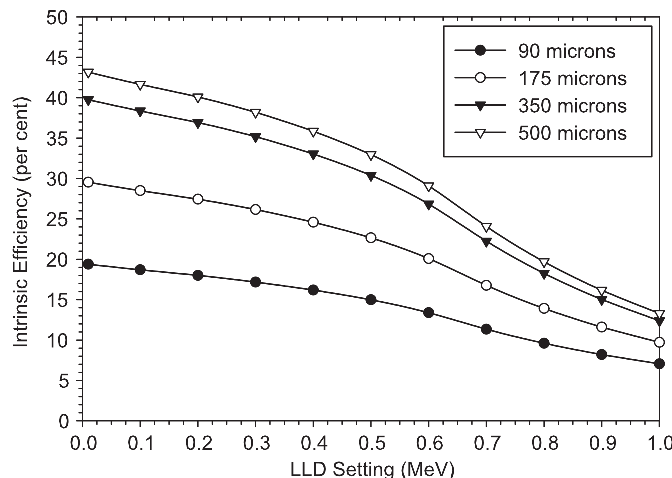

Fig. 22. Comparison of intrinsic efficiencies as a function of pillar height for the pillar design. The unit cell dimensions are 25 μm and the reactive material surrounding the pillars is ^{6}LiF. Pillar diameters are 12.5 microns.

Table 6
Efficiencies for cylindrical silicon pillars of diameter D and height H surrounded by ^{6}LiF in a unit cell of width W_{cell}.

D/W_{cell}	Cell width W_{cell} (μm)				
	20	40	60	80	100
	Pillar height $H = 90\,\mu m$				
0.10	3.79	3.93	4.10	4.04	3.89
0.20	6.61	7.02	5.96	5.27	4.81
0.30	11.90	9.48	7.47	6.36	5.67
0.40	16.49	11.60	8.91	7.40	6.46
0.50	19.14	13.30	10.29	8.38	7.21
0.60	20.37	14.58	11.36	9.31	7.90
0.70	19.76	15.07	11.93	9.96	8.52
0.80	17.33	14.38	11.76	9.97	8.70
0.90	13.52	12.10	10.52	8.98	7.93
	Pillar height $H = 175\,\mu m$				
0.10	3.10	3.39	3.67	3.55	3.31
0.20	7.98	8.62	6.82	5.69	4.92
0.30	16.99	12.86	9.48	7.63	6.48
0.40	24.80	16.58	12.05	9.54	7.97
0.50	29.44	19.66	14.60	11.40	9.45
0.60	31.74	22.05	16.68	13.24	10.89
0.70	31.04	23.21	17.97	14.67	12.26
0.80	27.33	22.44	18.07	15.07	12.95
0.90	21.36	19.06	16.41	13.84	12.08
	Pillar height $H = 350\,\mu m$				
0.10	2.41	2.83	3.23	3.07	2.72
0.20	9.37	10.24	7.69	6.09	5.03
0.30	22.12	16.27	11.51	8.91	7.29
0.40	33.18	21.59	15.25	11.69	9.49
0.50	39.80	26.06	18.94	14.45	11.69
0.60	43.20	29.58	22.05	17.19	13.89
0.70	42.40	31.42	24.06	19.42	16.01
0.80	37.41	30.56	24.41	20.20	17.22
0.90	29.25	26.06	22.33	18.74	16.27
	Pillar height $H = 500\,\mu m$				
0.10	2.19	2.65	3.09	2.90	2.52
0.20	9.83	10.77	7.98	6.24	5.07
0.30	23.82	17.40	12.18	9.34	7.56
0.40	35.97	23.26	16.31	12.41	10.01
0.50	43.25	28.20	20.39	15.47	12.44
0.60	47.01	32.09	23.85	18.51	14.89
0.70	46.18	34.15	26.09	21.00	17.27
0.80	40.76	33.26	26.52	21.91	18.65
0.90	31.88	28.40	24.31	20.36	17.66

Neutrons are incident normally on the detector surface, and the LLD cutoff energy is 300 keV.

with a $D/W_{cell} = 0.60$ is approaching the best design for all perforation depths. In such a case the detector would have 12-μm-diameter pillars with 8-μm-thick absorber regions between the pillars at the narrowest points.

3.4. Discussions and comparisons of tabulated data

Tables 1–6 list calculated efficiencies for the three perforated designs for various perforation depths for an LLD setting of 300 keV to discriminate against background gamma rays. The 300 keV LLD setting is 5 times larger than the energy at which photoelectric absorption equals Compton scattering in Si. Further, a gamma ray must have at least 465 keV of energy to produce a 300 keV Compton electron in Si. A few direct comparisons of ^{10}B backfilled perforated neutron detectors are shown in Figs. 25–31, and a few direct comparisons of ^{6}LiF backfilled perforated neutron detectors are shown in Figs. 32–35.

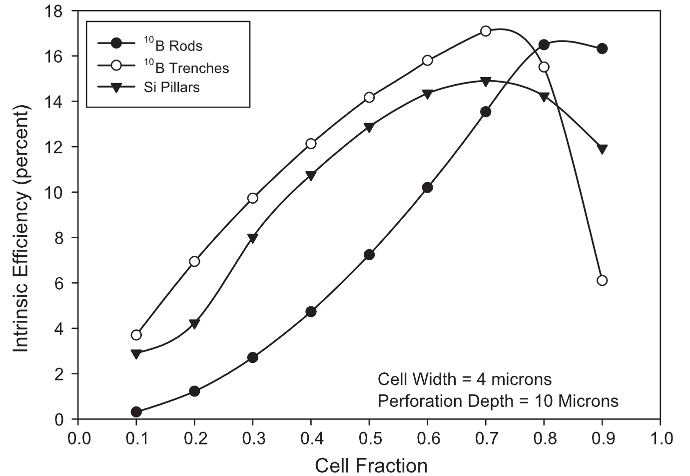

Fig. 25. Comparison of intrinsic thermal-neutron detection efficiencies as a function of feature size, as measured by its cell fraction, for hole, trench and pillar designs with unit cell dimensions of 4 μm and feature depths of 10 μm backfilled with ^{10}B. The LLD was set at 300 keV for all calculations.

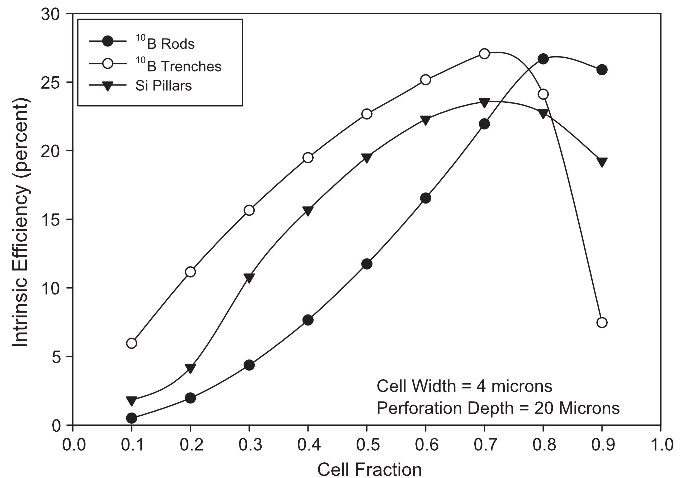

Fig. 26. Comparison of intrinsic thermal-neutron detection efficiencies as a function of feature size, as measured by its cell fraction, for hole, trench and pillar designs with unit cell dimensions of 4 μm and feature depths of 20 μm backfilled with ^{10}B. The LLD was set at 300 keV for all calculations.

3.4.1. ^{10}B comparisons

The calculated efficiencies are shown in Fig. 25 for devices with 4-μm unit cells with 10-μm-deep etched features backfilled with ^{10}B for various feature sizes measured as a fraction of the cell dimension. For instance, a feature with a 0.4 cell fraction value is equal to (0.4)(4) = 1.6 μm. Hence, the data points for a 0.4 cell fraction correspond to 1.6-μm-diameter holes, 1.6-μm-wide trenches, and 1.6-μm-diameter pillars.

It should be noticed that the trench design has higher efficiency than both the pillar design and the hole design for cell fractions ranging from 0.1 up to 0.8. At a cell fraction of 0.8, the hole design has the highest efficiency. Further, the trench design has the highest possible efficiency, peaking near 17% at a cell fraction of 0.7. The same trend appears in Figs. 26 and 27, where the features depths are 20 and 40 μm, respectively. For perforations 20 μm deep, the highest ε_{tn} is 27%, achieved by the trench design at a cell fraction of 0.7. For perforations 40 μm deep, the highest ε_{tn} is 36.75%, achieved by the trench design again at a cell fraction of about 0.7. Notice that the hole design achieves nearly as high an efficiency, namely, 36.6% at a cell fraction of about 0.8.

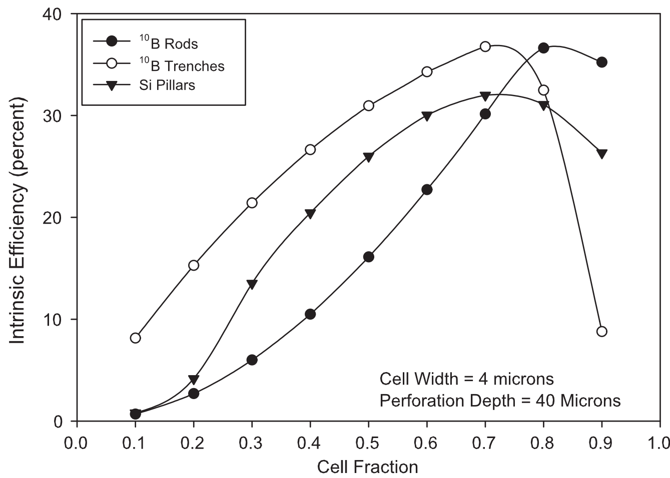

Fig. 27. Comparison of intrinsic thermal-neutron detection efficiencies as a function of feature size, as measured by its cell fraction, for hole, trench and pillar designs with unit cell dimensions of 4 μm and feature depths of 40 μm backfilled with ^{10}B. The LLD was set at 300 keV for all calculations.

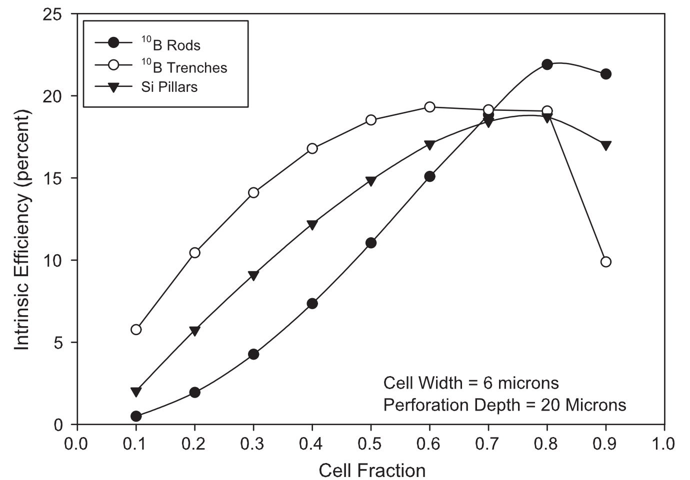

Fig. 29. Comparison of intrinsic thermal-neutron detection efficiencies as a function of feature size, as measured by its cell fraction, for hole, trench and pillar designs with unit cell dimensions of 6 μm and feature depths of 20 μm backfilled with ^{10}B. The LLD was set at 300 keV for all calculations.

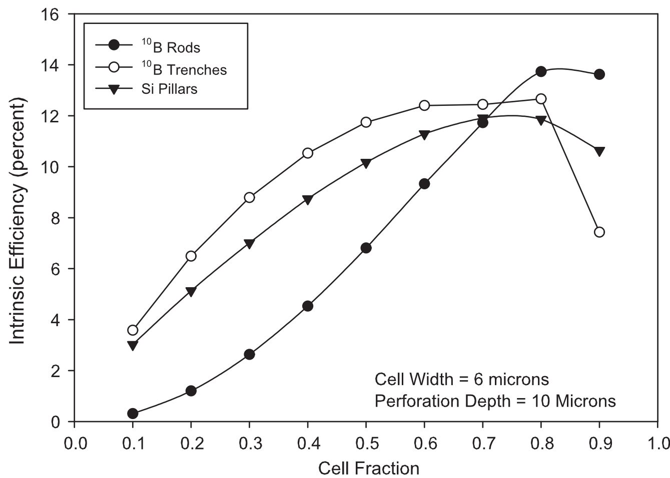

Fig. 28. Comparison of intrinsic thermal-neutron detection efficiencies as a function of feature size, as measured by its cell fraction, for hole, trench and pillar designs with unit cell dimensions of 6 μm and feature depths of 10 μm backfilled with ^{10}B. The LLD was set at 300 keV for all calculations.

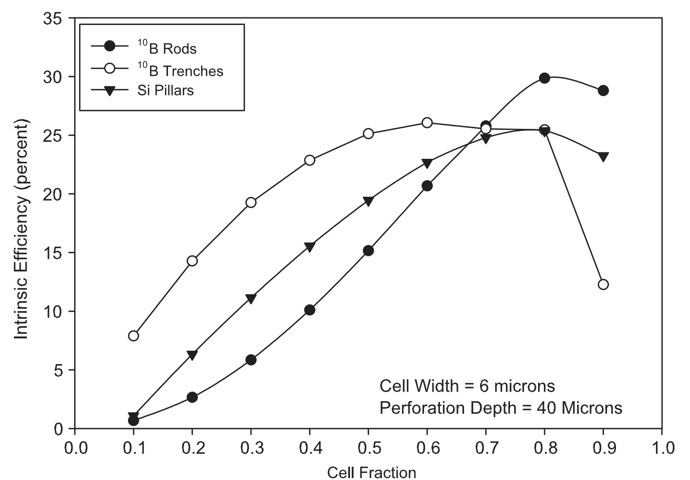

Fig. 30. Comparison of intrinsic thermal-neutron detection efficiencies as a function of feature size, as measured by its cell fraction, for hole, trench and pillar designs with unit cell dimensions of 6 μm and feature depths of 40 μm backfilled with ^{10}B. The LLD was set at 300 keV for all calculations.

Notice also that the pillar design intrinsic efficiency is always lower than either the trench or the hole design intrinsic efficiency. As detailed in the next section, the reduced performance of the pillar design is a consequence resulting from a considerable fraction of ^{10}B(n, α)^{7}Li reaction ions leaving less than 300 keV of energy in the pillars.

In Fig. 28 the expected efficiencies are shown for devices with 6-μm cell dimensions with 10-μm-deep etched features backfilled with ^{10}B as a function of feature size as a fraction of the cell dimension. The trench design has higher efficiency than both the pillar design and the hole design for cell fractions ranging from 0.1 up to 0.75. At a cell fraction of 0.75, the hole design has the highest efficiency. Further, it is the hole design has the highest possible efficiency, peaking near 13.73% at a cell fraction of 0.8. The same trend appears in Figs. 29 and 30, where the features depths are 20 and 40 μm, respectively. For perforations 20 μm deep, the highest ε_{tn} is 21.9%, achieved by the hole design at a cell fraction of 0.8. For perforations 40 μm deep, the highest ε_{tn} is 29.8%, achieved by the hole design again at a cell fraction of 0.8. The pillar design intrinsic efficiency is always lower than either the trench or the hole design intrinsic efficiency. These same

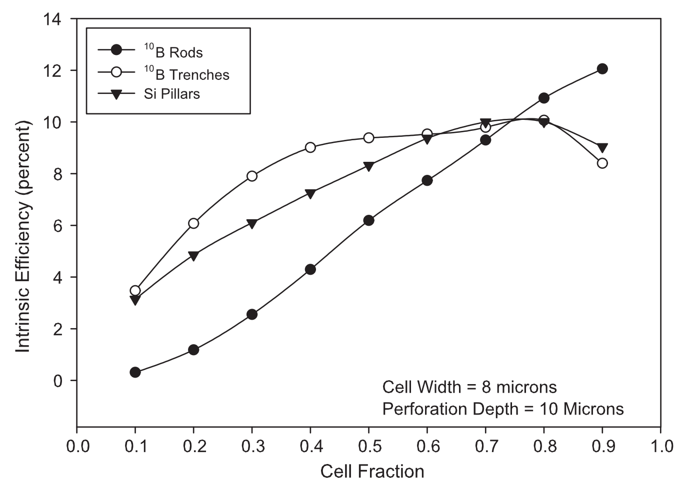

Fig. 31. Comparison of intrinsic thermal-neutron detection efficiencies as a function of feature size, as measured by its cell fraction, for hole, trench and pillar designs with unit cell dimensions of 8 μm and feature depths of 10 μm backfilled with ^{10}B. The LLD was set at 300 keV for all calculations.

trends continue for larger dimensions as evident from Tables 1, 3, and 5, however there are specific larger geometries for cell widths $\geqslant 8\,\mu m$ in which each perforation type (hole, trench, pillar) is greatest. In all cases, the trench design dominates at cell fractions $\leqslant 0.6$, and the hole design dominates at cell fractions $\geqslant 0.8$, and the pillar design barely achieves higher efficiency than the hole or trench designs at a cell fraction near 0.7, as seen in Fig. 31. Overall, it is the hole design that achieves the highest efficiency for perforation cell widths $\geqslant 8\,\mu m$, yet as the cell width increases, the maximum achievable ε_{tn} decreases.

Design optimization requires that a balance be struck between the minimum cell width and perforation size that can actually be fabricated, and the amount of semiconductor material that must be present adjacent to the neutron reactive material to absorb enough ion energy to exceed the required LLD setting.

3.4.2. ^{6}LiF *comparisons*

Fig. 32 shows the estimated efficiencies for devices with 20-μm cell dimensions with 90-μm-deep etched features backfilled with ^{6}LiF as a function of feature size as a fraction of the cell dimension. The trench design has the highest achievable efficiency, compared to the pillar and hole designs, peaking above 22% at a cell fractions between 0.7 and 0.8. The pillar design has a higher achievable efficiency in the cell fraction range between 0.25 and 0.62, being bypassed by the trench design at a cell fraction of 0.62. The hole design yields the lowest efficiency except at high cell fraction values exceeding 0.83. A similar trend is seen in Fig. 33, in which, again, the trench design has the highest achievable efficiency, peaking above 34.5% at a cell fractions between 0.7 and 0.8. The pillar design has a higher achievable efficiency in the cell fraction range between 0.3 and 0.62, being bypassed by the trench design at a cell fraction above 0.62. The hole design yields the lowest efficiency in all cases except at high cell-fraction values exceeding 0.82. Tables 2, 4, and 6 present efficiencies for deeper perforation values of 300 and 500 μm; however, these depths are difficult to achieve (although not impossible) and, hence, are not plotted here.

The estimated efficiencies are shown in Fig. 34 for devices with 40-μm-cell dimensions with 90-μm-deep etched features backfilled with ^{6}LiF as a function of feature size. The trench design has

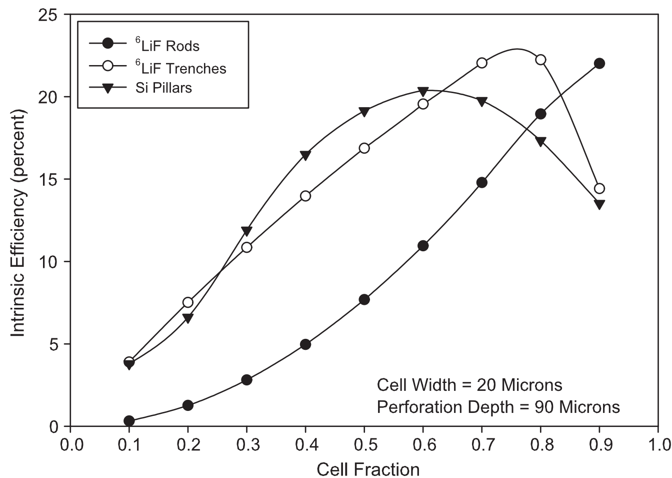

Fig. 32. Comparison of intrinsic thermal-neutron detection efficiencies as a function of feature size, as measured by its cell fraction, for hole, trench and pillar designs with unit cell dimensions of 20 μm and feature depths of 90 μm backfilled with ^{7}LiF. The LLD was set at 300 keV for all calculations.

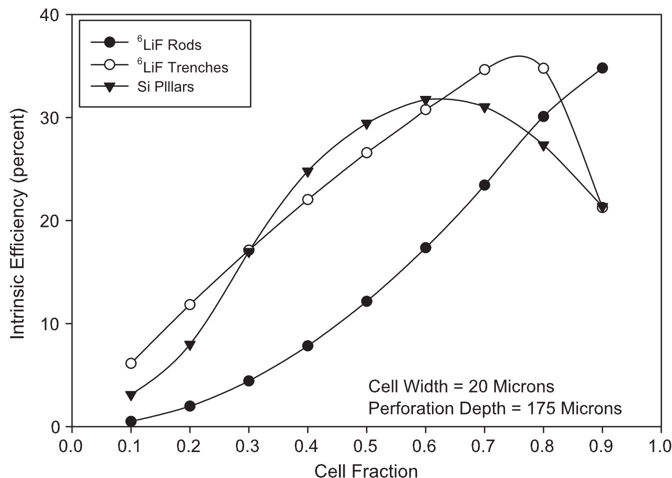

Fig. 33. Comparison of intrinsic thermal-neutron detection efficiencies as a function of feature size, as measured by its cell fraction, for hole, trench and pillar designs with unit cell dimensions of 20 μm and feature depths of 175 μm backfilled with ^{7}LiF. The LLD was set at 300 keV for all calculations.

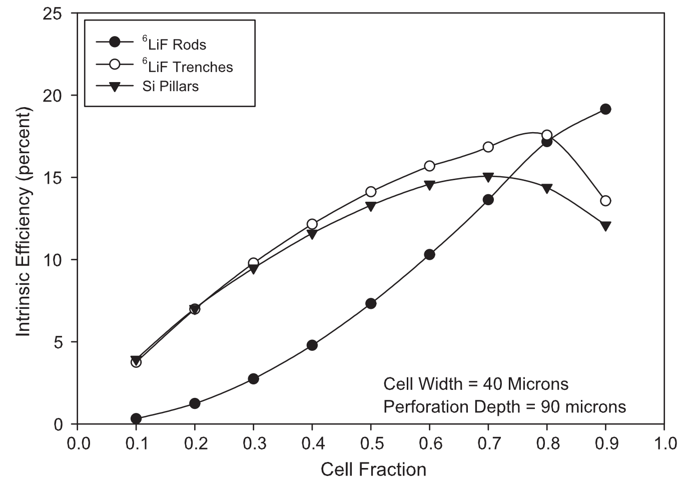

Fig. 34. Comparison of intrinsic thermal-neutron detection efficiencies as a function of feature size, as measured by its cell fraction, for hole, trench and pillar designs with unit cell dimensions of 40 μm and feature depths of 90 μm backfilled with ^{7}LiF. The LLD was set at 300 keV for all calculations.

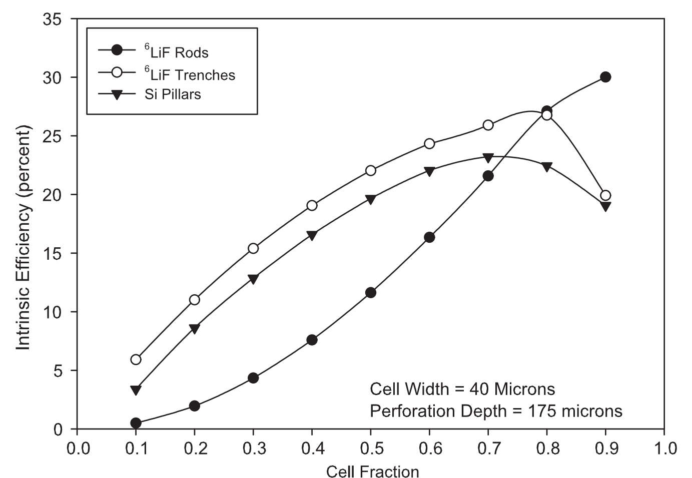

Fig. 35. Comparison of intrinsic thermal-neutron detection efficiencies as a function of feature size, as measured by its cell fraction, for hole, trench and pillar designs with unit cell dimensions of 40 μm and feature depths of 175 μm backfilled with ^{7}LiF. The LLD was set at 300 keV for all calculations.

the highest achievable efficiency at all values between a cell fraction of 0.3 and 0.8, with a maximum efficiency of 17.6%. The pillar and trench designs have almost identical efficiencies for cell fractions between 0.1 and 0.25, and the hole design efficiency exceeds both the trench and pillar designs at cell fractions exceeding 0.81, rising up to 19.1% at a cell fraction of 0.9. A similar trend is seen in Fig. 35 in which the trench design has the highest achievable efficiency at all cell fractions between 0.1 and 0.8, peaking at approximately 26.8% efficiency. The hole design yields the lowest efficiency in all cell fraction cases below 0.73, where it matches the pillar design, and becomes dominant at a cell fraction of 0.8, where it increases above the trench design. The hole design can achieve an efficiency of 30% at a cell fraction of 0.9. Again, the calculations for deeper perforations of 300 and 500 μm, listed in Tables 2, 4, and 6 are not plotted, although they exhibit similar trends.

3.5. General spectral comparisons

Design optimization requires a balance between the minimum cell width and the size of the perforation features that can actually be fabricated and the amount of semiconductor material that must be present adjacent to the neutron reactive material to absorb enough ion energy to exceed the required LLD setting. The expected pulse height spectra from the devices can provide insight about the energy-deposition distribution that the reaction ions deposit in the silicon. Such spectra yield the expected efficiency as a function of the LLD setting. In this section, direct comparisons are made of the expected pulse height spectra for all three designs along with direct comparisons of the expected efficiencies as a function of the LLD settings.

3.5.1. Case 1: boron filled 4-μm-wide cells

To compare the results for the three designs, certain general traits of spectral features and efficiencies should be noted. First, the spectral features for the pillar design are concentrated in the low energy region, mainly because the full energy of the reactions cannot be deposited in the semiconductor. Rather, only a portion of the reaction energy can be deposited in the Si pillars, a problem that increases as the diameter of the pillars are reduced below the ion ranges. By contrast, the spectral features for the hole design are shifted to the higher energies, primarily because more ion energy can be absorbed in the semiconductor. The trench design falls between these two extremes, with a more evenly distributed

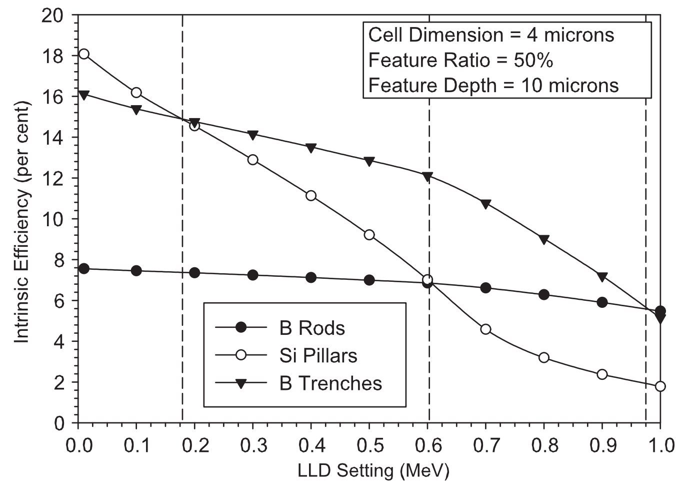

Fig. 37. Comparison of intrinsic efficiencies as a function of the LLD setting for hole, trench and pillar designs with unit cell dimensions of 4 μm and feature ratios of 50%. The feature depths are 10 μm and are backfilled with ^{10}B.

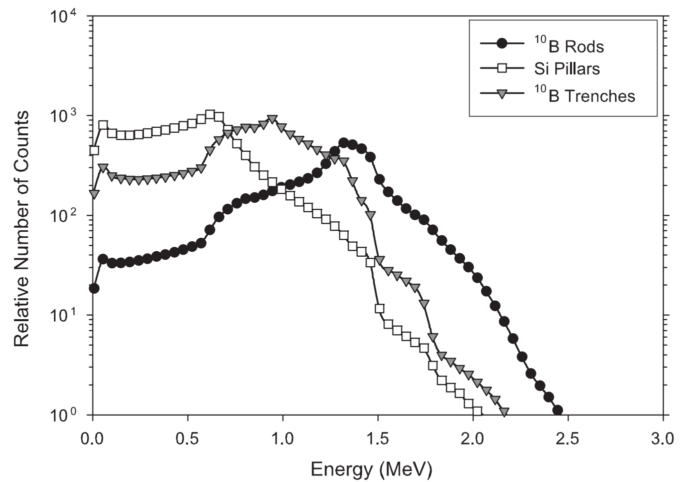

Fig. 38. Comparison of energy-deposition spectra for hole, trench and pillar designs with unit cell dimensions of 4 μm and feature ratios of 50%. The feature depths are 20 μm and are backfilled with ^{10}B.

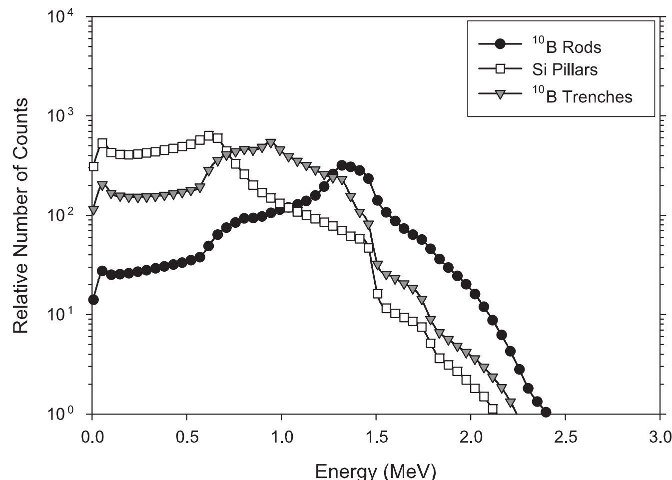

Fig. 36. Comparison of energy-deposition spectra for hole, trench and pillar designs with unit cell dimensions of 4 μm and feature ratios of 50%. The feature depths are 10 μm and are backfilled with ^{10}B.

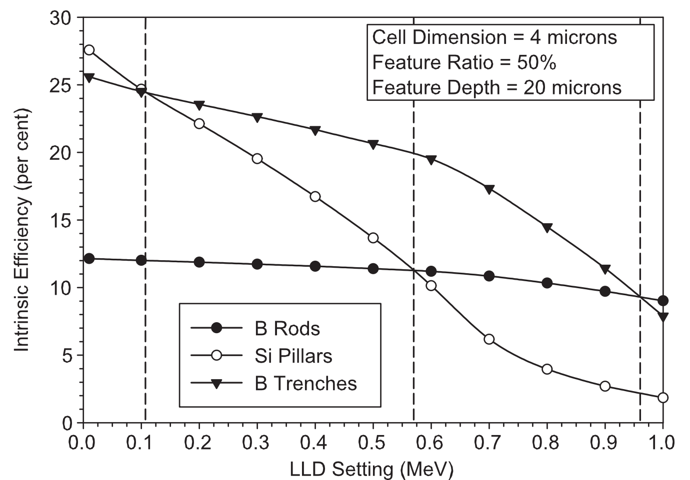

Fig. 39. Comparison of intrinsic efficiencies as a function of the LLD setting for hole, trench and pillar designs with unit cell dimensions of 4 μm and feature ratios of 50%. The feature depths are 20 μm and are backfilled with ^{10}B.

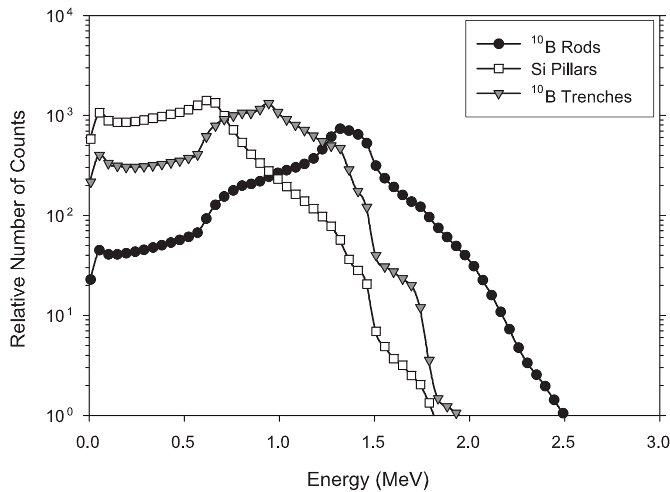

Fig. 40. Comparison of energy-deposition spectra for hole, trench and pillar designs with unit cell dimensions of 4 μm and feature ratios of 50%. The feature depths are 40 μm and are backfilled with ^{10}B.

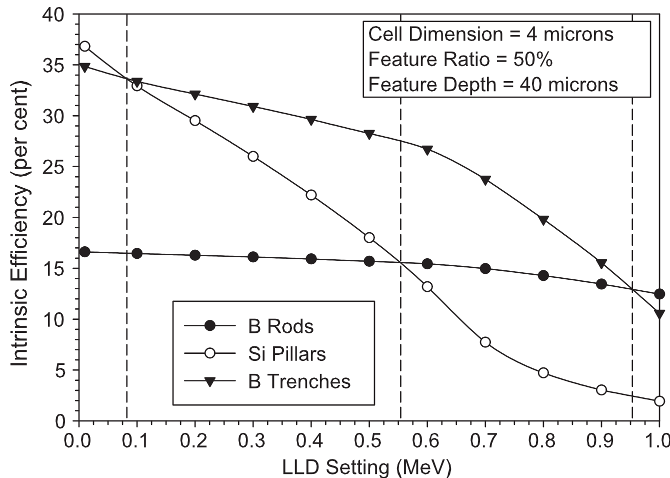

Fig. 41. Comparison of intrinsic efficiencies as a function of the LLD setting for hole, trench and pillar designs with unit cell dimensions of 4 μm and feature ratios of 50%. The feature depths are 40 μm and are backfilled with ^{10}B.

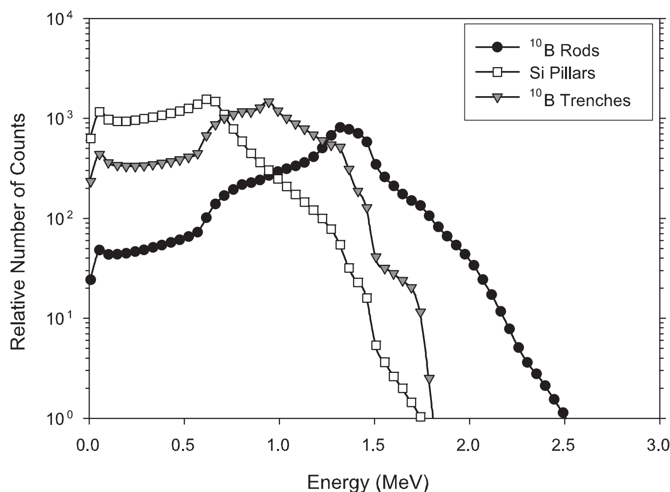

Fig. 42. Comparison of energy-deposition spectra for hole, trench and pillar designs with unit cell dimensions of 4 μm and feature ratios of 50%. The feature depths are 60 μm and are backfilled with ^{10}B.

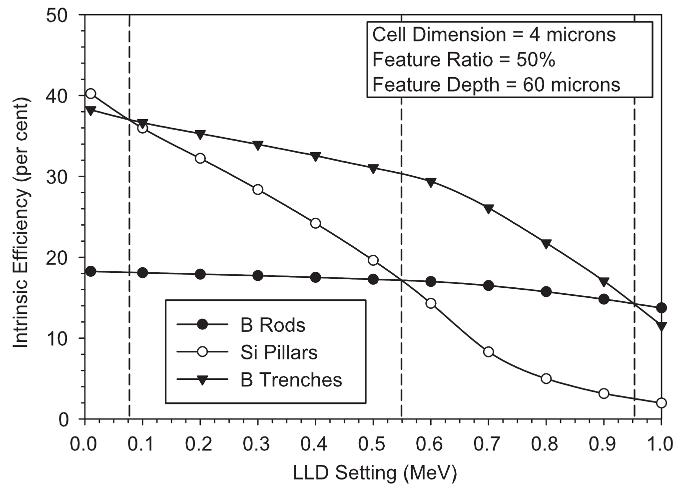

Fig. 43. Comparison of intrinsic efficiencies as a function of the LLD setting for hole, trench and pillar designs with unit cell dimensions of 4 μm and feature ratios of 50%. The feature depths are 60 μm and are backfilled with ^{10}B.

energy-deposition spectrum. The spectral features for the three ^{10}B-filled designs are depicted for feature depths of 10, 20, 40 and 60 μm in Figs. 36, 38, 40, and 42, respectively.

In most cases neutron emissions are accompanied by gamma-ray emissions, and users must also consider electronic noise. As a result, a LLD is used to reject unwanted pulses that arise from electronic noise and/or background gamma radiation. Figs. 37, 39, 41, and 43 show the expected efficiencies for hole, trench and pillar designs as a function of LLD setting for various feature depths. From Fig. 37 it is seen that, for 10-μm-deep features filled with ^{10}B, the pillar design has a slightly higher efficiency (18.2% at LLD = 0) than the trench design (16.2% at LLD = 0), and much higher than the hole design (7.6% at LLD = 0) for LLD settings below 180 keV. Yet, at LLD settings above 180 keV, the trench design is superior to both the pillar and hole designs, mainly because the ion energies absorbed in the pillar design are primarily in the lower region of the spectrum; hence, the LLD has a greater effect on eliminating counts from neutron events. Notice also that the trench design is less susceptible to efficiency changes as the LLD is increased, and the hole design shows almost no change in efficiency for LLD settings below 600 keV. For example, with an LLD setting at 300 keV, the trench design efficiency falls to 14.5% efficiency (an absolute negative change of 1.7% efficiency) and the pillar design efficiency falls to 13% efficiency (an absolute negative change of 5.2% efficiency); however, the efficiency of the hole design falls to only 7.3% (an absolute negative change of 0.3% efficiency). Further, the pillar design efficiency is actually lower than the hole design efficiency for LLD settings above 600 keV, dropping below 7% efficiency.

From these results, it is seen that the hole design offers the lowest intrinsic efficiency, primarily because it has the smallest amount of neutron reactive material in the detectors; however, it provides the best stability for various LLD settings, showing an average change in intrinsic efficiency of only 0.12% per 100 keV increment below 600 keV. The trench design offers the best intrinsic efficiency and good stability for various LLD settings, showing an average intrinsic efficiency change of 0.67% per 100 keV increment below 600 keV. Finally, the pillar design yields efficiencies generally below that of the trench design and also has the worst stability for various LLD settings, showing an average intrinsic efficiency change of 1.84% per 100 keV increment below 600 keV. At LLD settings above 600 keV, the hole design intrinsic efficiency out performs the pillar design.

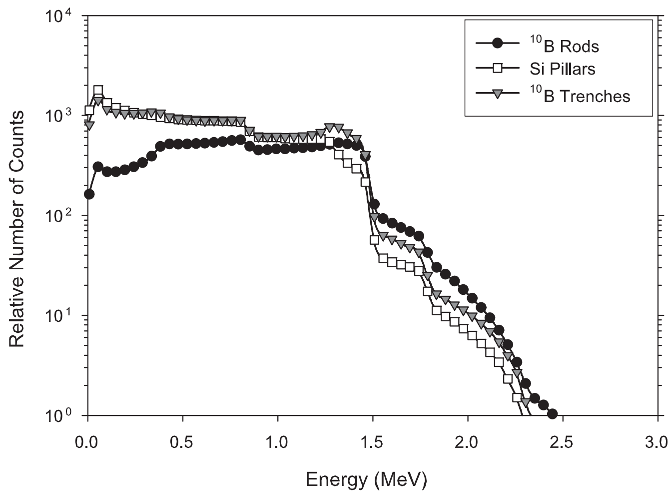

Fig. 44. Comparison of energy-deposition spectra for hole, trench and pillar designs with unit cell dimensions of 8 μm and feature ratios of 50%. The feature depths are 10 μm and are backfilled with ^{10}B.

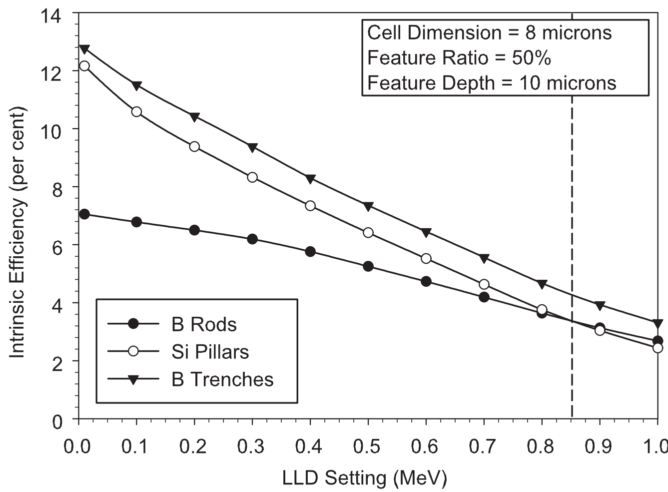

Fig. 45. Comparison of intrinsic efficiencies as a function of the LLD setting for hole, trench and pillar designs with unit cell dimensions of 8 μm and feature ratios of 50%. The feature depths are 10 μm and are backfilled with ^{10}B.

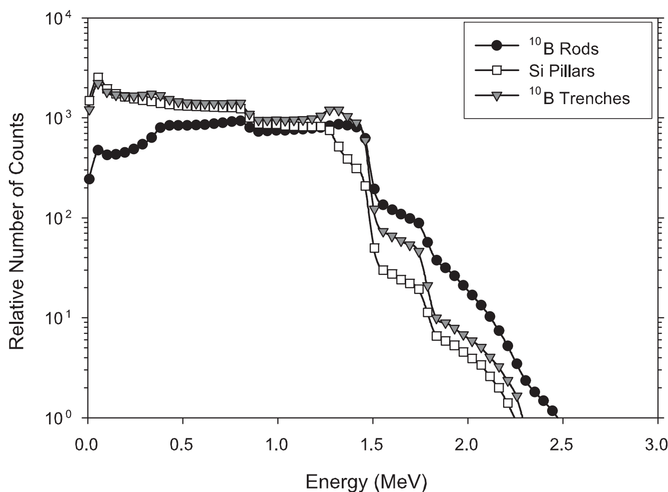

Fig. 46. Comparison of energy-deposition spectra for hole, trench and pillar designs with unit cell dimensions of 8 μm and feature ratios of 50%. The feature depths are 20 μm and are backfilled with ^{10}B.

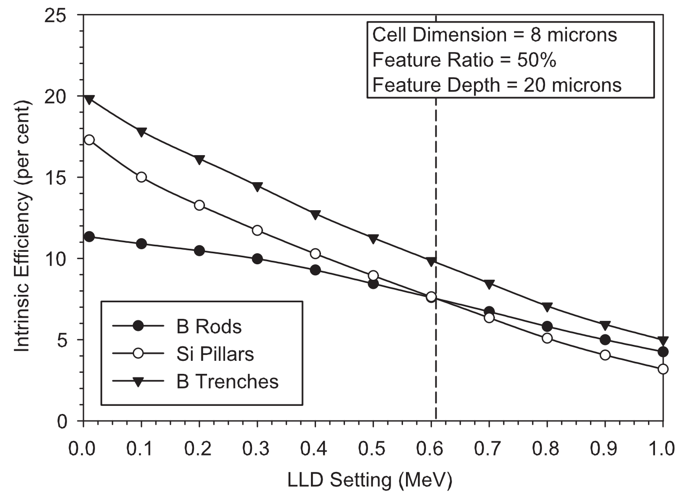

Fig. 47. Comparison of intrinsic efficiencies as a function of the LLD setting for hole, trench and pillar designs with unit cell dimensions of 8 μm and feature ratios of 50%. The feature depths are 20 μm and are backfilled with ^{10}B.

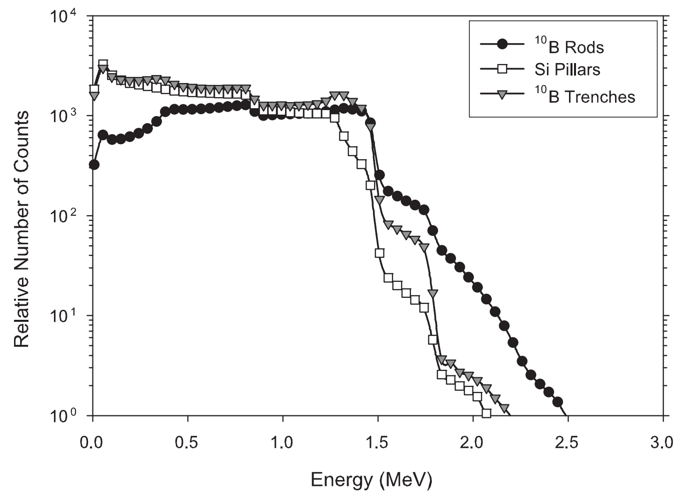

Fig. 48. Comparison of energy-deposition spectra for hole, trench and pillar designs with unit cell dimensions of 8 μm and feature ratios of 50%. The feature depths are 40 μm and are backfilled with ^{10}B.

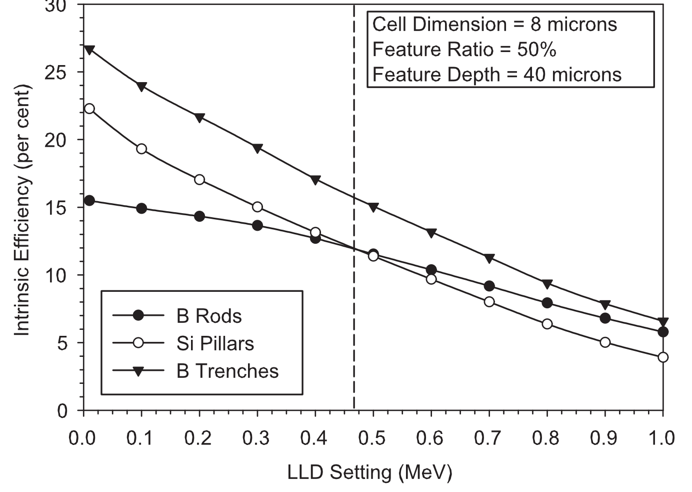

Fig. 49. Comparison of intrinsic efficiencies as a function of the LLD setting for hole, trench and pillar designs with unit cell dimensions of 8 μm and feature ratios of 50%. The feature depths are 40 μm and are backfilled with ^{10}B.

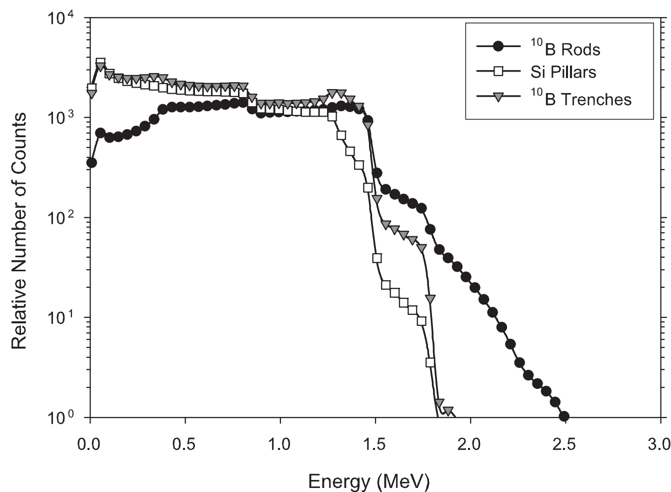

Fig. 50. Comparison of energy-deposition spectra for hole, trench and pillar designs with unit cell dimensions of 8 μm and feature ratios of 50%. The feature depths are 60 μm and are backfilled with ^{10}B.

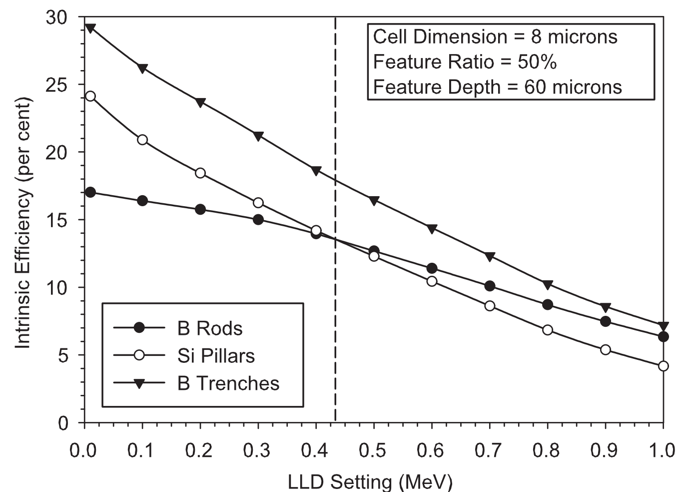

Fig. 51. Comparison of intrinsic efficiencies as a function of the LLD setting for hole, trench and pillar designs with unit cell dimensions of 8 μm and feature ratios of 50%. The feature depths are 60 μm and are backfilled with ^{10}B.

It should be noticed that these spectral and efficiency trends for the 4-μm cell are observed for deeper perforations as can be seen from Figs. 38 through 43 although efficiency cross over values between the pillar designs and the trench or hole designs are different, and the change in efficiency as a function of the LLD setting increases. For instance, for 60 micron deep features, the average change in intrinsic efficiency for the hole design is 0.21% per 100 keV increment below 700 keV. The trench design offers better intrinsic efficiency and acceptable stability for various LLD settings, showing an average intrinsic efficiency change of 1.48% per 100 keV increment below 700 keV. The pillar design yields efficiencies below that of the trench design and again the worst stability for various LLD settings, showing an average intrinsic efficiency change of 4.32% per 100 keV increment in the range below 600 keV.

3.5.2. *Case 2: boron filled 8-μm-wide cells*

At 8-μm-cell dimensions with feature fractions of 50%, the three designs produce very similar energy-deposition spectra because self-absorption of the ion energy in the ^{10}B converter material becomes similar for holes, trenches and pillars. The hole design still has slightly fewer counts in the lower energy channels, while the trench and pillar designs are almost identical. The spectral features for the three ^{10}B-filled designs are depicted for feature depths of 10, 20, 40 and 60 μm in Figs. 44, 46, 48, and 50, respectively. Figs. 45, 47, 49, and 51 show the expected efficiencies for hole, trench and pillar designs as a function of LLD setting for various feature depths. Here it is noticed that in all cases and for all LLD settings that it is the trench design that delivers the highest efficiency. All designs show appreciable decreases in efficiency as a function of LLD setting, with the trench and pillar design being nearly the same and the hole design being slightly less susceptible to increasing LLD values. Further, the efficiencies are lower than the 4-μm-cell dimension cases.

For 10-μm-deep perforations, the hole design offers the lowest efficiency primarily due to the lower overall neutron reactive absorber in the detectors, yet provides better stability for various LLD settings. The trench design offers the best efficiency, yet shows appreciable decrease (nearly linear) in efficiency as the LLD setting is increased from 0 to 1 MeV. The pillar design has efficiencies lower than the trench design, and also below the hole design at LLD settings above 850 keV, and shows a nearly linear decrease in efficiency as the LLD is increased from 0 to 1 MeV; hence, the pillar design offers little advantage over either the trench of hole designs. It should be noticed that these spectral and efficiency trends for the 8-μm cell are observed for deeper perforations of 20, 40, and 60 μm as can be seen from Figs. 46 through 51 although efficiency cross over values are somewhat different.

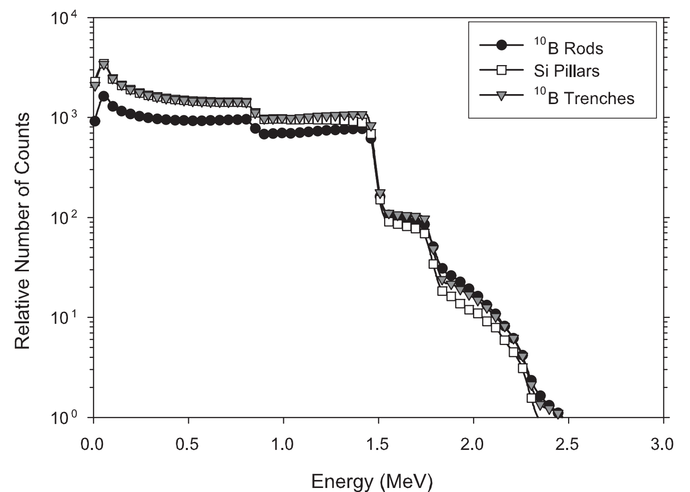

Fig. 52. Comparison of energy-deposition spectra for hole, trench and pillar designs with unit cell dimensions of 12 μm and feature ratios of 50%. The feature depths are 10 μm and are backfilled with ^{10}B.

3.5.3. *Case 3: boron filled 12-μm-wide cells*

At 12-μm-cell dimensions with feature fractions of 50%, the three designs again have similar energy-deposition spectra as seen from Figs. 52, 54, 56, and 58 for feature depths of 10, 20, 40 and 60 μm, respectively. The hole design still has slightly fewer counts in the lower energy channels, yet is hardly different than the trench and pillar designs.

Figs. 53, 55, 57, and 59 show the corresponding expected efficiencies for hole, trench and pillar designs as a function of LLD setting (in MeV) for various feature depths. Here it is noticed that in all cases and LLD levels that it is the trench design that delivers the highest efficiency. All designs show appreciable decreases in efficiency as a function of LLD setting, with the trench and pillar design being nearly the same and the hole design being slightly less susceptible. Further, the efficiencies are lower than the 4- and 8-μm-cell dimension cases. Although the efficiencies are still higher than those of planar coated diodes [6], it can be concluded

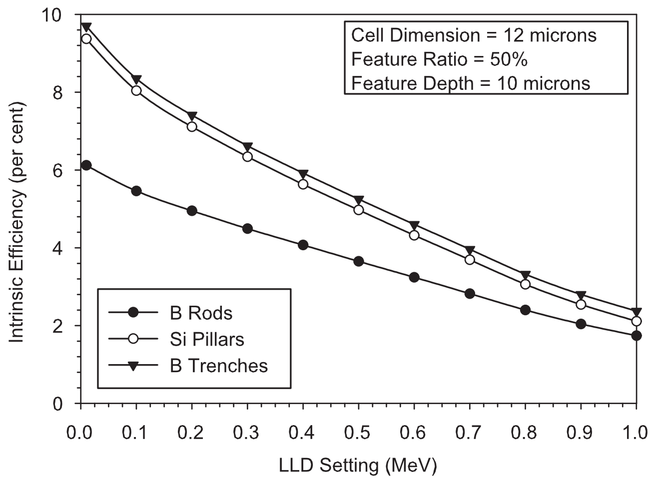

Fig. 53. Comparison of intrinsic efficiencies as a function of the LLD setting for hole, trench and pillar designs with unit cell dimensions of 12 μm and feature ratios of 50%. The feature depths are 10 μm and are backfilled with ^{10}B.

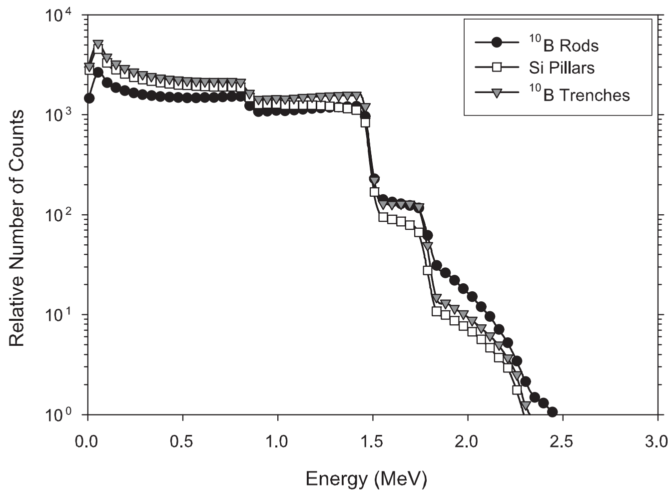

Fig. 54. Comparison of energy-deposition spectra for hole, trench and pillar designs with unit cell dimensions of 12 μm and feature ratios of 50%. The feature depths are 20 μm and are backfilled with ^{10}B.

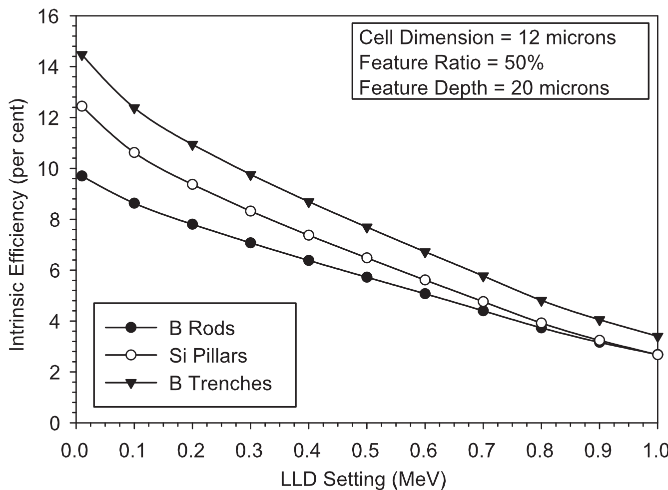

Fig. 55. Comparison of intrinsic efficiencies as a function of the LLD setting for hole, trench and pillar designs with unit cell dimensions of 12 μm and feature ratios of 50%. The feature depths are 20 μm and are backfilled with ^{10}B.

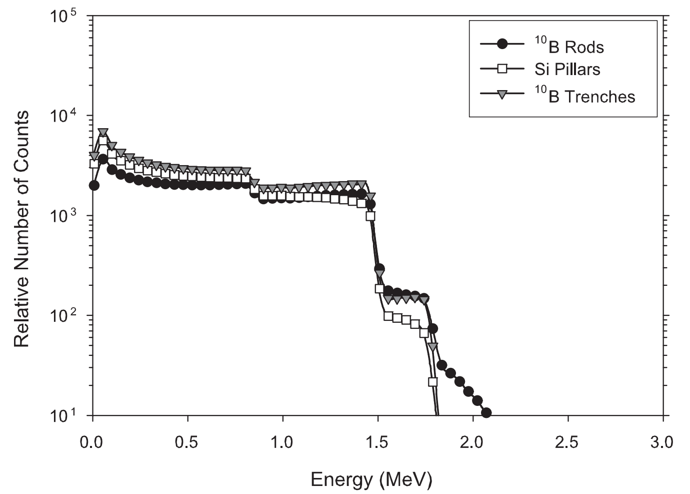

Fig. 56. Comparison of energy-deposition spectra for hole, trench and pillar designs with unit cell dimensions of 12 μm and feature ratios of 50%. The feature depths are 40 μm and are backfilled with ^{10}B.

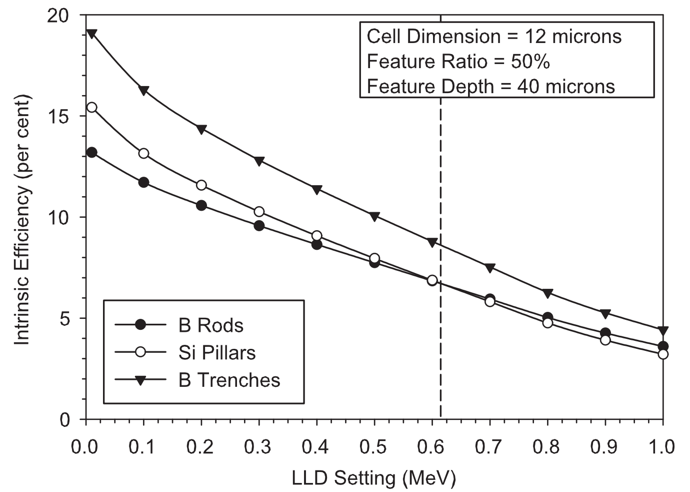

Fig. 57. Comparison of intrinsic efficiencies as a function of the LLD setting for hole, trench and pillar designs with unit cell dimensions of 12 μm and feature ratios of 50%. The feature depths are 40 μm and are backfilled with ^{10}B.

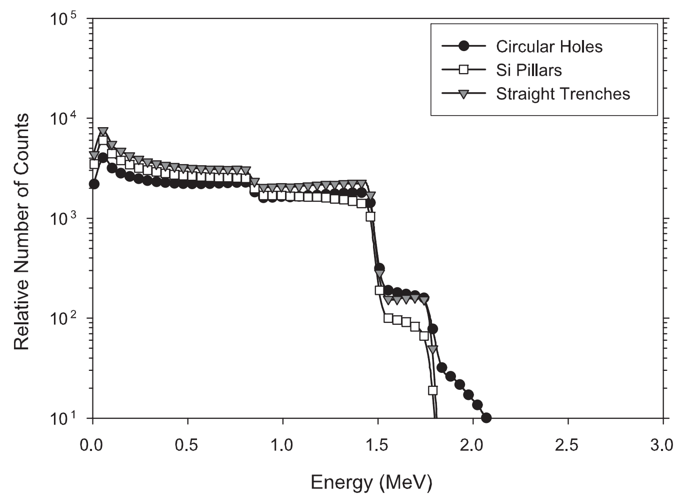

Fig. 58. Comparison of energy-deposition spectra for hole, trench and pillar designs with unit cell dimensions of 12 μm and feature ratios of 50%. The feature depths are 60 μm and are backfilled with ^{10}B.

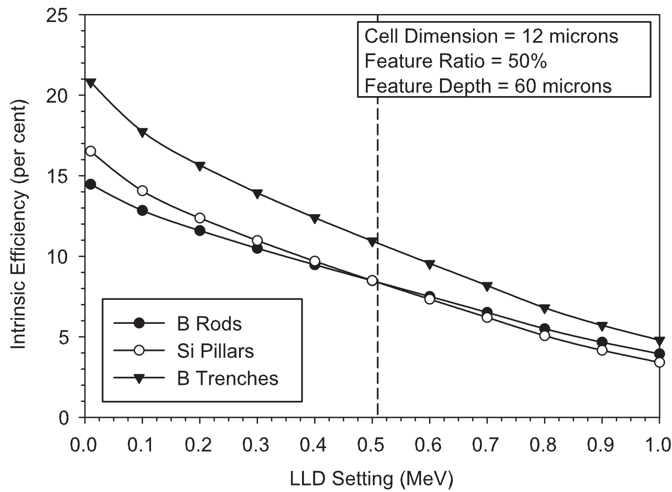

Fig. 59. Comparison of intrinsic efficiencies as a function of the LLD setting for hole, trench and pillar designs with unit cell dimensions of 12 μm and feature ratios of 50%. The feature depths are 60 μm and are backfilled with ^{10}B.

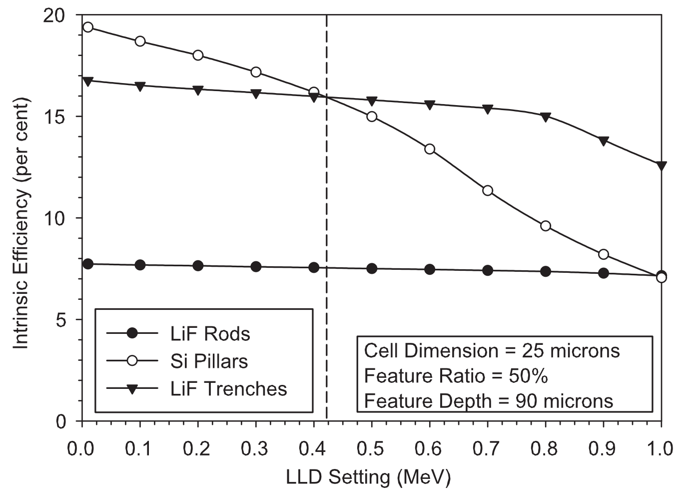

Fig. 61. Comparison of intrinsic efficiencies as a function of the LLD setting for hole, trench and pillar designs with unit cell dimensions of 25 μm and feature ratios of 50%. The feature depths are 90 μm and are backfilled with ^{6}LiF.

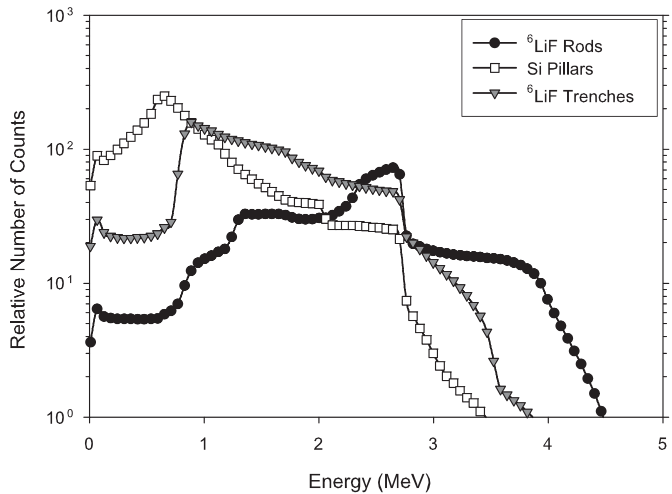

Fig. 60. Comparison of energy-deposition spectra for hole, trench and pillar designs with unit cell dimensions of 25 μm and feature ratios of 50%. The feature depths are 90 μm and are backfilled with ^{6}LiF.

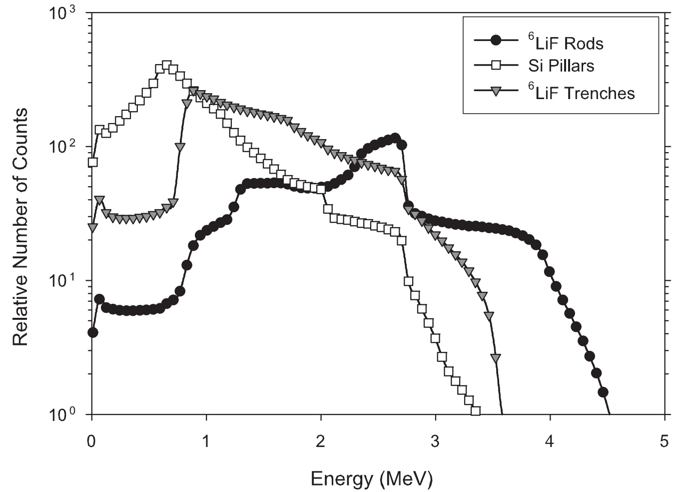

Fig. 62. Comparison of energy-deposition spectra for hole, trench and pillar designs with unit cell dimensions of 25 μm and feature ratios of 50%. The feature depths are 175 μm and are backfilled with ^{6}LiF.

that these larger cell dimensions do not offer optimum results for ε_{tn}, and ^{10}B-filled devices should be fabricated with smaller cell dimensions to obtain higher efficiencies (see Figs. 52–59).

3.5.4. Case 4: LiF filled 25-μm-wide cells

The spectral features for the three 25-μm-cell ^{6}LiF-filled designs are depicted for feature depths of 90, 175, 350, and 500 μm in Figs. 60, 62, 64, and 66, respectively. The spectral features of the three designs are quite different, sometimes more than an order of magnitude in both the high and low energy regions. It is seen that the spectral features for the pillar design are concentrated in the low energy region, again because the full energy of the reactions ions cannot be deposited in the small semiconductor regions, much as occurs with the 4-μm-cell ^{10}B-filled designs. Instead, only a portion of the ion energy is deposited in the Si pillars, a problem that increases as the diameter of the pillars is reduced below the effective ion range. More important, the spectral features for both the trench and hole designs are shifted to the higher spectral energies, much more so than the corresponding ^{10}B-filled designs, a result that more ion

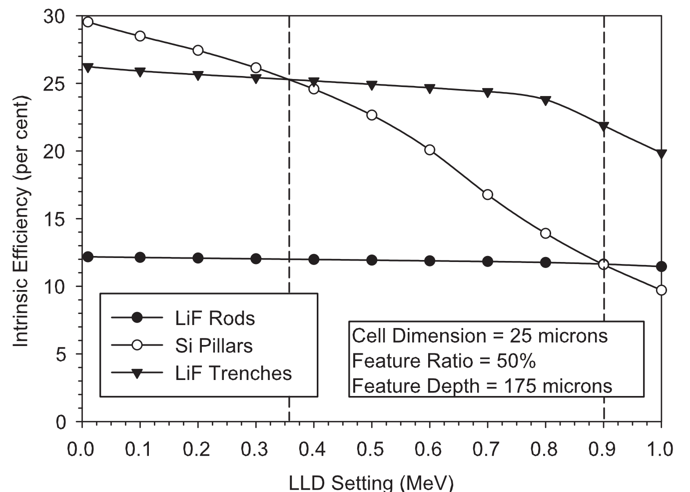

Fig. 63. Comparison of intrinsic efficiencies as a function of the LLD setting for hole, trench and pillar designs with unit cell dimensions of 25 μm and feature ratios of 50%. The feature depths are 175 μm and are backfilled with ^{6}LiF.

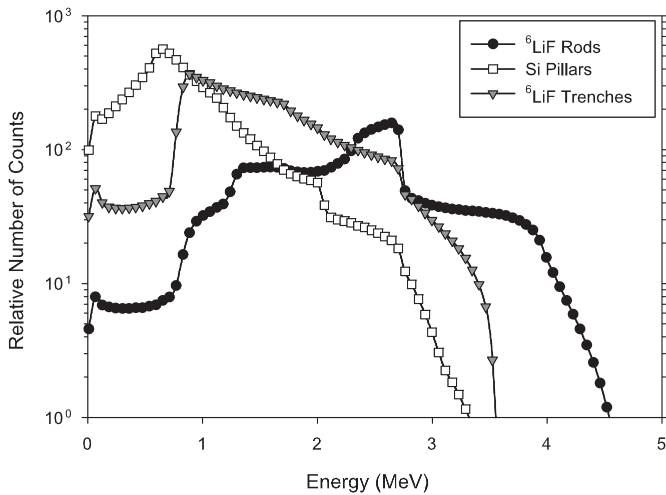

Fig. 64. Comparison of energy-deposition spectra for hole, trench and pillar designs with unit cell dimensions of 25 μm and feature ratios of 50%. The feature depths are 350 μm and are backfilled with ^{6}LiF.

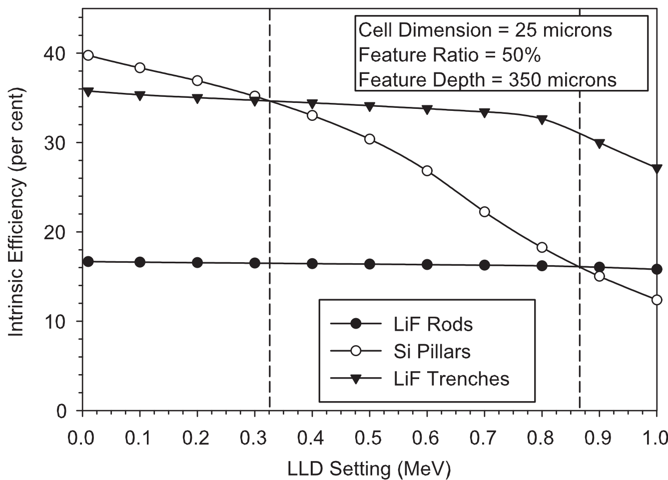

Fig. 65. Comparison of intrinsic efficiencies as a function of the LLD setting for hole, trench and pillar designs with unit cell dimensions of 25 μm and feature ratios of 50%. The feature depths are 350 μm and are backfilled with ^{6}LiF.

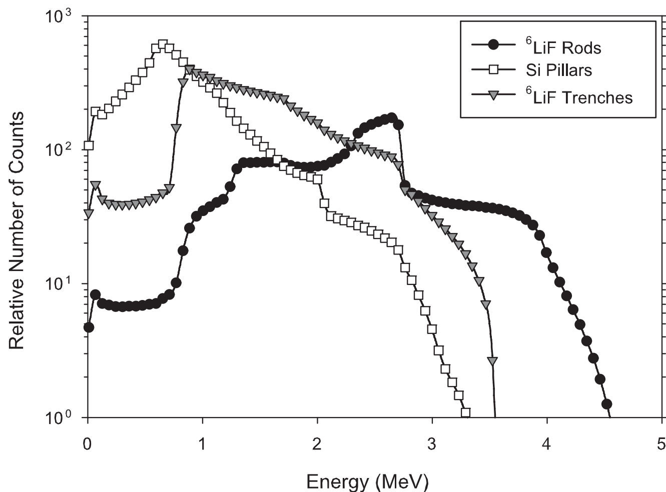

Fig. 66. Comparison of energy-deposition spectra for hole, trench and pillar designs with unit cell dimensions of 25 μm and feature ratios of 50%. The feature depths are 500 μm and are backfilled with ^{6}LiF.

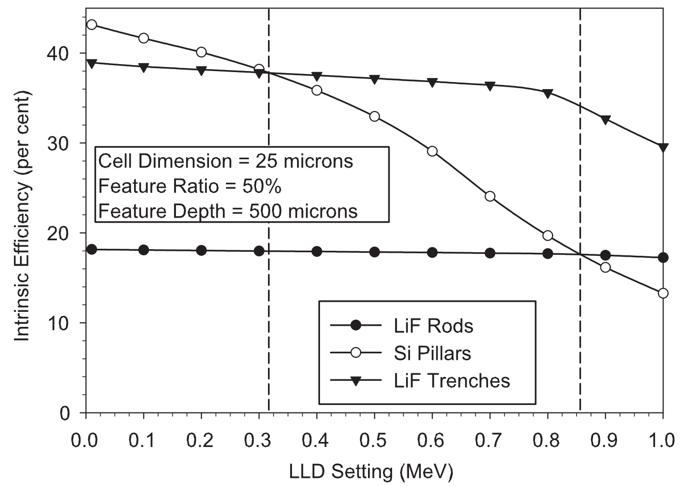

Fig. 67. Comparison of intrinsic efficiencies as a function of the LLD setting for hole, trench and pillar designs with unit cell dimensions of 25 μm and feature ratios of 50%. The feature depths are 500 μm and are backfilled with ^{6}LiF.

energy is absorbed from both ions in the semiconductor. Further, there are obvious valleys in the pulse height spectra for the trench and hole designs for energies below 0.8 MeV.

To discriminate against unwanted pulses produced from electronic noise and background gamma radiation an LLD setting >0 must be applied to detectors, thereby, rejecting the lower energy spectral counts. Figs. 61, 63, 65, and 67 show the expected efficiencies for hole, trench and pillar designs as a function of LLD setting (in MeV) for various feature depths. Notice from Fig. 61, which shows the case for 90-μm-deep features filled with ^{6}LiF, the pillar design has a higher efficiency (19.4% at LLD $=0$) than the trench design (16.8% at LLD $=0$), and much higher than the hole design (7.8% at LLD $=0$). At LLD settings above 420 keV, the efficiency for the pillar design falls below that of the trench design, mainly because energy deposition for the pillar design is primarily in the lower region of the spectrum and increasing the LLD setting has a greater effect on eliminating spectral counts. Notice also that the trench design shows almost no change in efficiency for LLD settings below 700 keV, remaining near 16.5% ε_{tn}. Further, the hole design shows almost no change in efficiency for LLD settings below 800 keV, remaining near 7.8% (see Figs. 60–67).

As an example, for an LLD setting at 300 keV the pillar design efficiency is reduced to 17.5% (an absolute negative change of 1.9% efficiency), the trench design efficiency is reduced to only 16.4% (an absolute negative change of 0.4% efficiency), and the hole design is reduced to only 7.7% (an absolute negative change of 0.1% efficiency).

From these results, it can be concluded that the hole design offers the lowest detector efficiency primarily because of the smaller amount of neutron reactive absorber in the detectors compared to the other designs. However, it provides the best stability for various LLD settings, showing an average change in intrinsic efficiency of only 0.06% per 100 keV increment below 1 MeV. The trench design offers the good intrinsic efficiency and excellent stability for various LLD settings, showing an average intrinsic efficiency change of 0.19% per 100 keV increment below 700 keV. Finally, the pillar design yields the highest efficiencies at LLD settings below 420 keV, but the worst stability for various LLD settings, showing an average intrinsic efficiency change of 1.15% per 100 keV increment below 700 keV. At LLD settings above 420 keV, the trench design intrinsic efficiency out performs the pillar design. It should be noticed that these trends are observed for all design cases depicted for 25-μm-cell dimensions, although the actual efficiencies and cross over values do differ.

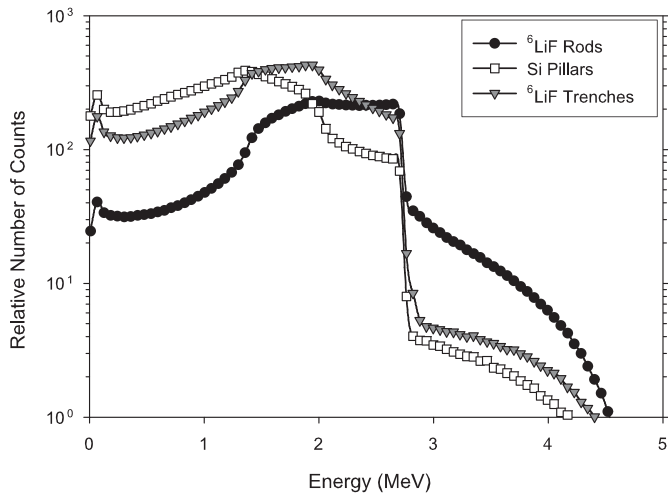

Fig. 68. Comparison of energy-deposition spectra for hole, trench and pillar designs with unit cell dimensions of 50 μm and feature ratios of 50%. The feature depths are 90 μm and are backfilled with ^{6}LiF.

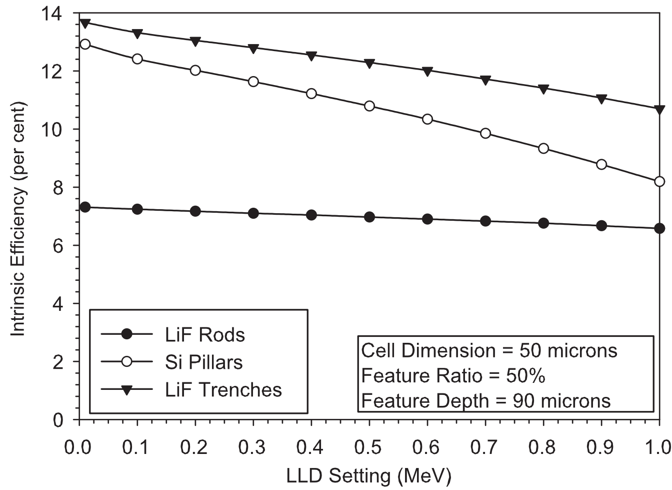

Fig. 69. Comparison of intrinsic efficiencies as a function of the LLD setting for hole, trench and pillar designs with unit cell dimensions of 50 μm and feature ratios of 50%. The feature depths are 90 μm and are backfilled with ^{6}LiF.

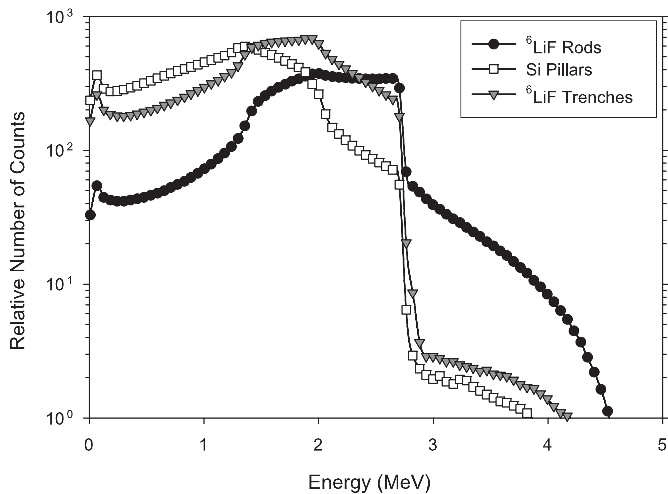

Fig. 70. Comparison of energy-deposition spectra for hole, trench and pillar designs with unit cell dimensions of 50 μm and feature ratios of 50%. The feature depths are 175 μm and are backfilled with ^{6}LiF.

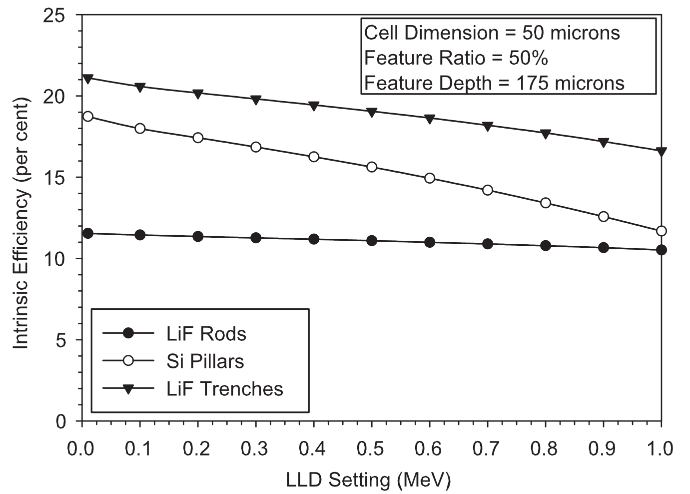

Fig. 71. Comparison of intrinsic efficiencies as a function of the LLD setting for hole, trench and pillar designs with unit cell dimensions of 50 μm and feature ratios of 50%. The feature depths are 175 μm and are backfilled with ^{6}LiF.

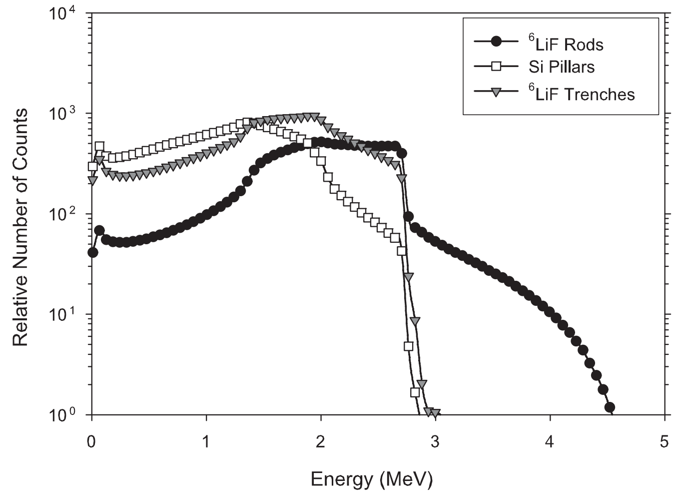

Fig. 72. Comparison of energy-deposition spectra for hole, trench and pillar designs with unit cell dimensions of 50 μm and feature ratios of 50%. The feature depths are 350 μm and are backfilled with ^{6}LiF.

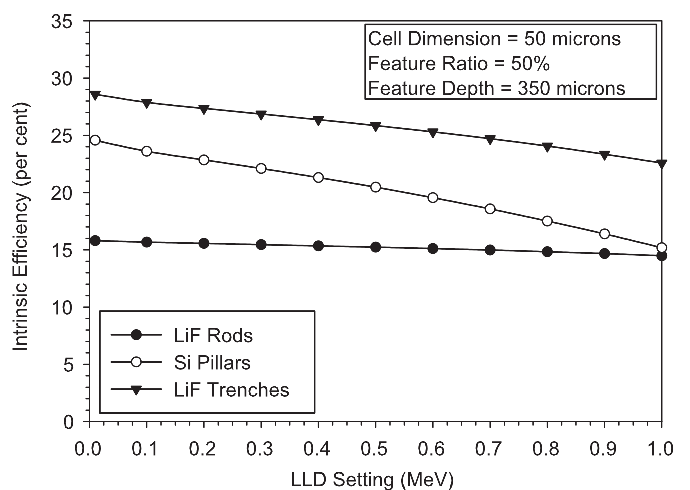

Fig. 73. Comparison of intrinsic efficiencies as a function of the LLD setting for hole, trench and pillar designs with unit cell dimensions of 50 μm and feature ratios of 50%. The feature depths are 350 μm and are backfilled with ^{6}LiF.

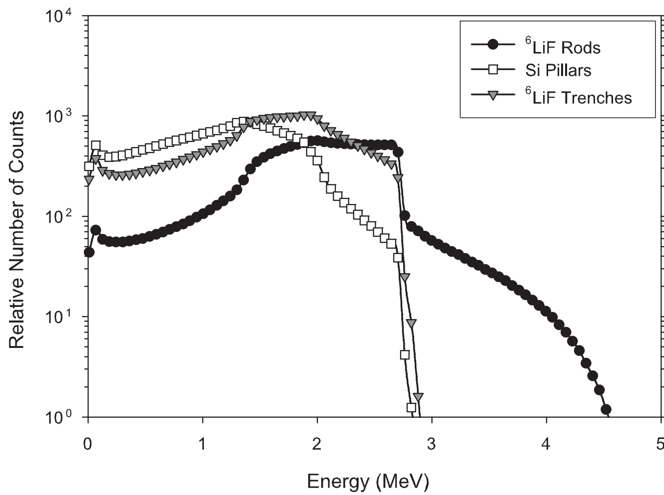

Fig. 74. Comparison of energy-deposition spectra for hole, trench and pillar designs with unit cell dimensions of 50 μm and feature ratios of 50%. The feature depths are 500 μm and are backfilled with ^{6}LiF.

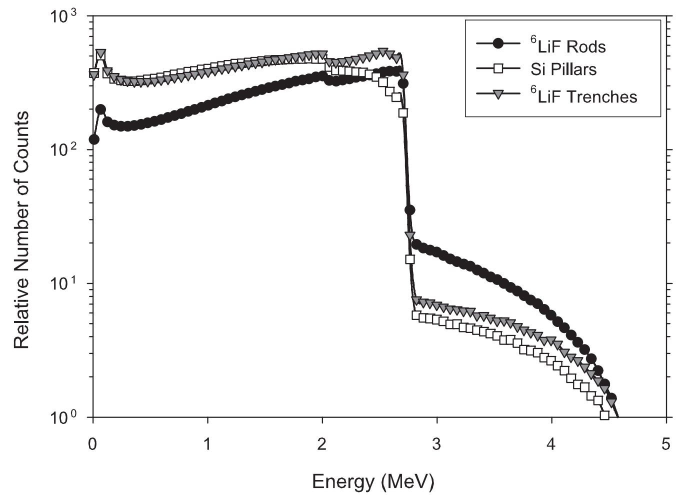

Fig. 76. Comparison of energy-deposition spectra for hole, trench and pillar designs with unit cell dimensions of 75 μm and feature ratios of 50%. The feature depths are 90 μm and are backfilled with ^{6}LiF.

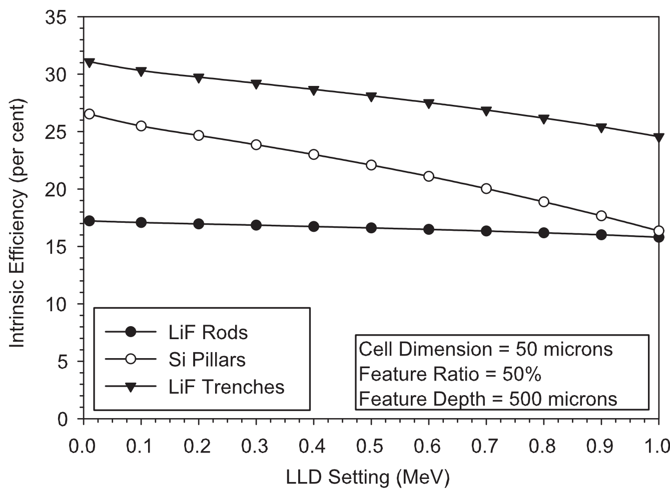

Fig. 75. Comparison of intrinsic efficiencies as a function of the LLD setting for hole, trench and pillar designs with unit cell dimensions of 50 μm and feature ratios of 50%. The feature depths are 500 μm and are backfilled with ^{6}LiF.

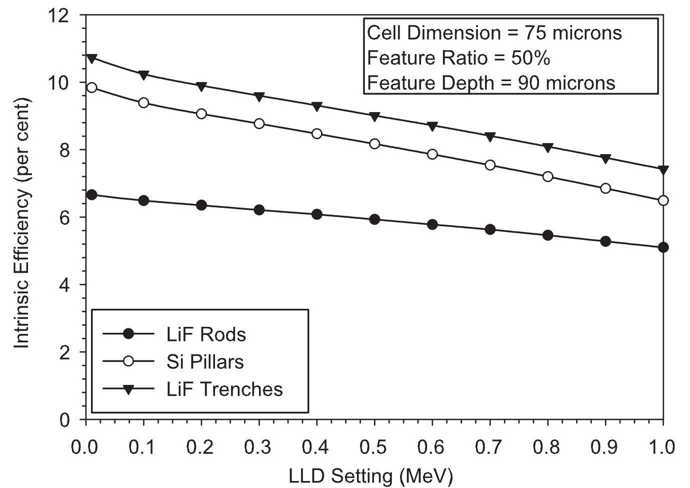

Fig. 77. Comparison of intrinsic efficiencies as a function of the LLD setting for hole, trench and pillar designs with unit cell dimensions of 75 μm and feature ratios of 50%. The feature depths are 90 μm and are backfilled with ^{6}LiF.

3.5.5. *Case 5: LiF filled 50-μm-wide cells*

At 50-μm-cell dimensions with feature fractions of 50%, the three detector designs again produce quite different energy-deposition spectra (see Figs. 68, 70, 72, and 74 for feature depths of 90, 175, 350, and 500 μm, respectively). Although the differences are not as severe as with the 25-μm designs, differences in the low and high energy portions of the energy-deposition spectra are quite noticeable.

Figs. 69, 71, 73, and 75 show the expected efficiencies for hole, trench and pillar designs as a function of LLD setting for various feature depths. Here it is noticed that in all cases and for all LLD settings between 0 and 1 MeV (1) it is the trench design that delivers the highest efficiency, (2) the hole design has the lowest efficiency, and (3) the pillar design has an efficiency intermediate between those of the hole and trench designs. As before, the pillar design exhibits the greatest decrease in efficiency with increasing LLD setting, followed by the trench design. The hole design is remarkably insensitive to changing LLD setting (see Figs. 68–75).

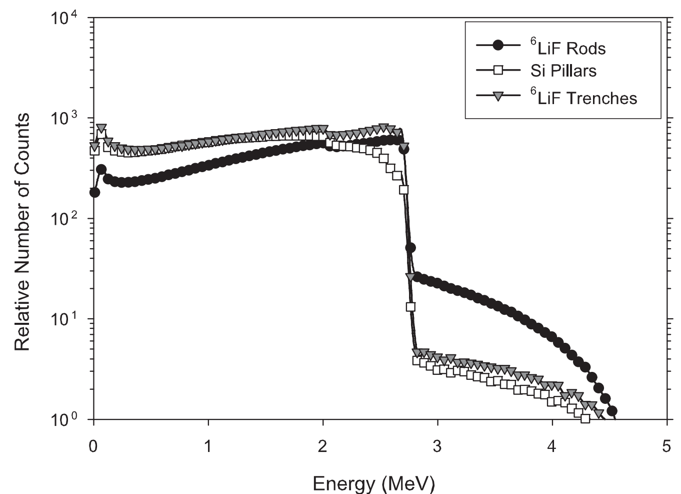

Fig. 78. Comparison of energy-deposition spectra for hole, trench and pillar designs with unit cell dimensions of 75 μm and feature ratios of 50%. The feature depths are 175 μm and are backfilled with ^{6}LiF.

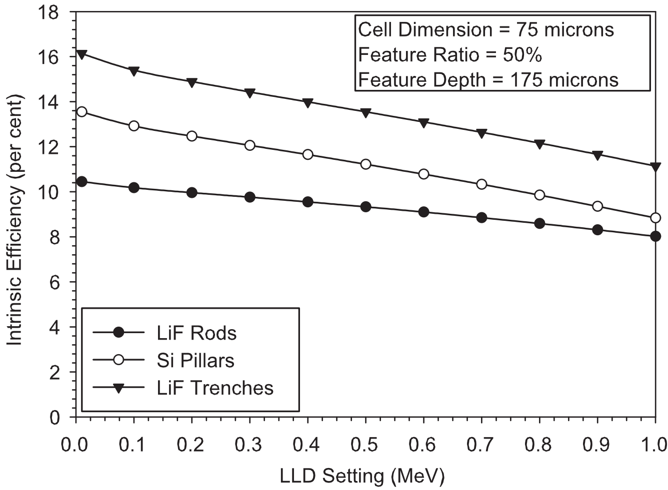

Fig. 79. Comparison of intrinsic efficiencies as a function of the LLD setting for hole, trench and pillar designs with unit cell dimensions of 75 μm and feature ratios of 50%. The feature depths are 175 μm and are backfilled with ^{6}LiF.

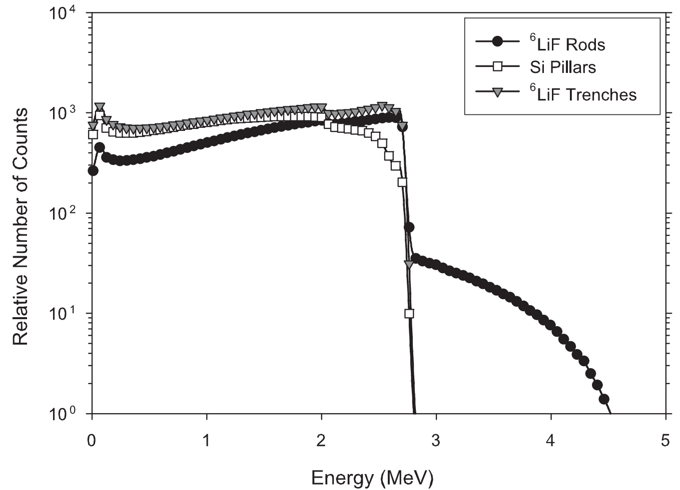

Fig. 82. Comparison of energy-deposition spectra for hole, trench and pillar designs with unit cell dimensions of 75 μm and feature ratios of 50%. The feature depths are 500 μm and are backfilled with ^{6}LiF.

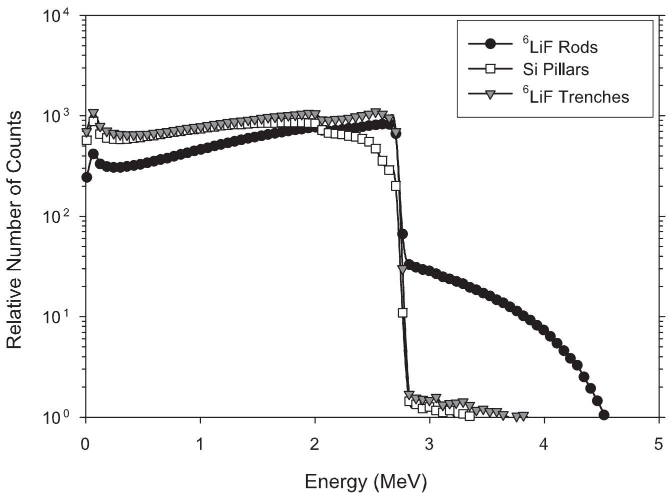

Fig. 80. Comparison of energy-deposition spectra for hole, trench and pillar designs with unit cell dimensions of 75 μm and feature ratios of 50%. The feature depths are 350 μm and are backfilled with ^{6}LiF.

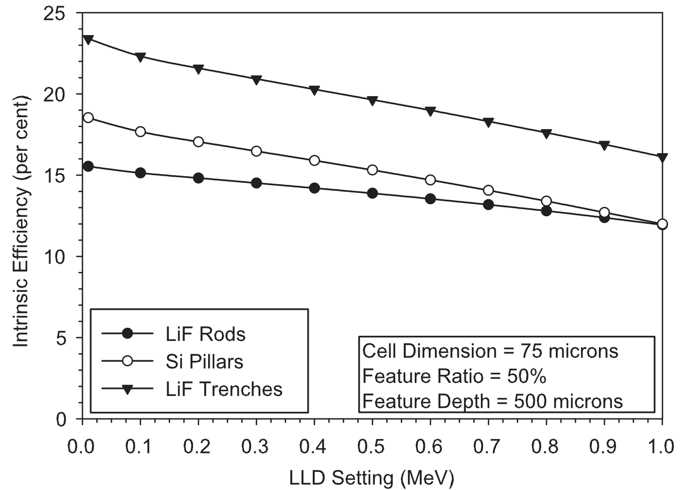

Fig. 83. Comparison of intrinsic efficiencies as a function of the LLD setting for hole, trench and pillar designs with unit cell dimensions of 75 μm and feature ratios of 50%. The feature depths are 500 μm and are backfilled with ^{6}LiF.

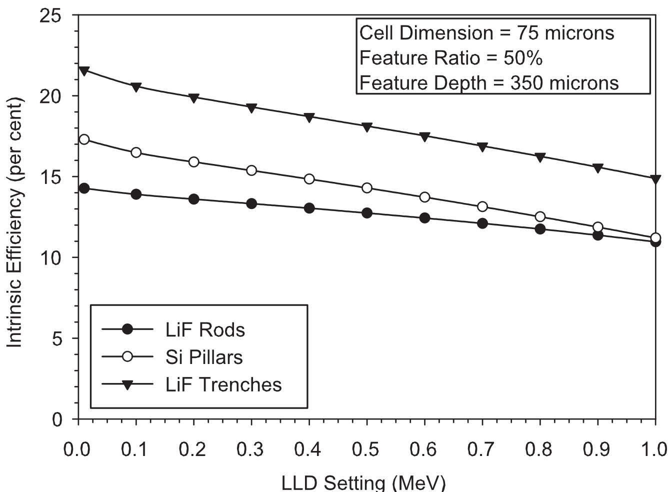

Fig. 81. Comparison of intrinsic efficiencies as a function of the LLD setting for hole, trench and pillar designs with unit cell dimensions of 75 μm and feature ratios of 50%. The feature depths are 350 μm and are backfilled with ^{6}LiF.

3.5.6. *Case 6: LiF filled 75-μm-wide cells*

At 75-μm-cell dimensions with feature fractions of 50%, the three detector designs produce energy-deposition spectra that now begin to resemble each other (see Figs. 76, 78, 80, and 82 for feature depths of 90, 175, 350, and 500 μm, respectively). For all perforation depths, the trench and pillar designs are very similar over the entire energy range. Although similar, the hole design shows decreased counts at the lower energies but more counts above the triton full-energy deposition channel at 2.73 MeV. A small spectral feature at the alpha full-energy deposition channel at 2.05 MeV is also clearly seen in all the spectra.

Figs. 77, 79, 81, and 83 show the expected efficiencies for hole, trench and pillar designs as a function of LLD setting for various feature depths. Again it is observed that in all cases and for all LLD levels between 0 and 1 MeV the trench design has the highest efficiency, the hole design has the lowest efficiency, and the efficiency of the pillar design is between those of the hole and trench designs. Here, the pillar design and the trench design exhibit almost the same decrease in efficiency with increasing LLD setting. The hole design, while still the least sensitive to LLD setting, begins to show a greater dependence on LLD setting than

those of the 25- and 50-μm-wide cells. Further, the efficiencies are lower than the 25- and 50-μm-cell dimension cases. Although the efficiencies are still higher than those of coated diodes [6], it can be concluded that these larger cell dimensions do not offer optimum results for ε_{tn}, and ^{6}LiF-filled devices should be fabricated with smaller cell dimensions to obtain better efficiencies (see Figs. 76–83).

4. Practical considerations

The calculated results presented here can be used in a general sense to understand trends in the performance of perforated semiconductor detectors. However, there are several phenomena that can alter the idealized pulse height spectra presented and, as a result, decrease the predicted efficiencies. The calculated efficiencies presented in this paper are the highest that can be obtained based on complete charge collection and ideal device operation. For instance, incomplete charge collection alters the predicted spectra by shifting counts to lower channels. Leakage currents increase system noise, forcing the LLD to be set higher. Dead regions near the etched surface of semiconductor will absorb some of the ion's energy before it reaches the semiconductor active region. Collectively, these effects cause a shift in the modeled trends that were studied in this work. These and other practical issues are discussed below.

4.1. *Feature sizes*

Although the presented calculations indicate that thermal-neutron detection efficiencies exceeding 35% can be reached with the trench, hole and pillar designs, the calculations are based on the assumption that all of the semiconductor material is sensitive to charged reaction ions and no dead layer regions exist between the Si perforation features and the neutron reactive conversion material. However, dead layers do exist between the converter and the Si material, typically due to oxidation and damage from the fabrication process. Further, very small features can be easily modeled but, in practice, are impractical to fabricate. As a result, these limitations, including etch dimensions, doping profiles, surface damage, and film backfill procedures, impose further restrictions that affect the overall achievable thermal-neutron detection efficiencies.

Submicron feature dimensions can be achieved with plasma reactive ion etching (RIE), yet it is important to understand whether such a structure can be converted into perforated diodes or detectors. RIE surface damage may range in thickness from several tens of nanometers to a few microns [18–20] and affects the performance of a device. Previous work clearly has shown that perforated structures have high leakage currents after plasma RIE processing [21]. To ameliorate leakage current problems for Si devices, the leakage current for perforated structures can be significantly reduced by using first selective doping and second by oxidation.

There is a general trend for all the geometries studied to increase the detector's efficiency as the feature sizes are reduced. This trend was shown to be the case elsewhere for the cylindrical hole and trench designs [7]. However, there is a minimal feature size that is practical to produce. For boron filled devices, the feature sizes must be on the same order of size as, or less than, the largest ion range from the ^{10}B(n,α)^{7}Li reaction. The maximum particle range is for alpha particles, and lies approximately between 3 and 4 μm [6]. However, the actual range and effective range,[1] which is used for the calculations, can be quite different. Larger semiconductor features take up surface area that reaction product particles cannot reach while reducing the amount of converter material in the device. Conversely, larger converter features increase the absorption of neutrons, but reaction products produced near the center of these regions undergo energy attenuation in the converter making them undetectable should they reach the semiconductor material. The same can be said for ^{6}LiF filled devices, with the change that the range for the energetic triton from the ^{6}Li(n,t)^{4}He reaction is approximately 43 μm in Si and 34 μm in LiF. Consequently, the feature sizes can be approximately 10 times larger for the ^{6}LiF filled devices than the features of ^{10}B filled devices.

As a practical consideration, the smallest feature geometry is one that can be manufactured. As feature sizes decrease, pn junction depths, surface damage and passivation steps become increasing important in determining the final performance of a device. Further, there must be an appropriate amount of "real estate" in the semiconductor to produce a low leakage current device. Devices manufactured with recessed buffer regions for the pn junction, in which the pn junction is not in contact with the etched region, have buffer regions between 1 and 2 μm [22,23]. Oxidation passivation is used to consume damage on the etched walls and provide insulation in the features; however, such treatment causes a dead region around the perforations that can extend from 0.3 to 2 μm [22,23]. Diffusion in the structures also causes the appearance of dead regions at the surface. Hence, the feature sizes must be large enough to permit these process steps while retaining enough semiconductor in the matrix to capture the energy of the reaction products.

The feature depth to width ratio, or aspect ratio, is another concern. Although the feature sizes for ^{6}LiF filled devices are far less challenging than those needed for ^{10}B filled devices, the necessary etching depths for high ε_{tn} exceed 100 μm. For deep etches, $>$300 μm, the aspect ratio exceeds 1:15, which can be achieved, yet this depth of the etched perforations increases the probability that damage on the walls compromises device performance, and requires that the depleted region extend much further into the substrate. At present, depths between 100 and 200 μm are used [22,23].

Conformal diffused junction devices eliminate the need for recessed junctions and oxide buffer regions. The device design has the pn junction conformally coating the inside of perforations [16,24,25]. Further, the depletion region is already present around the entire perforation. Although the capacitance should increase (from more surface area), thus far the resulting performance has improved over the recessed junction designs, yielding much lower leakage currents. Also, the experimentally observed spectral features are similar to those determined through analytical methods in the present work. At present, conformal designs with trenches etched to 150 μm have been fabricated and tested with encouraging results. Regardless, there will always be a thin "dead" region at the interface between the neutron absorber/converter material and the semiconductor; hence, some energy is inevitably lost as the reaction products cross the interface.

4.2. *Device processing*

For Si devices, the perforation wall damage can be further reduced by postprocess oxidation [26]. Although there is some indication that oxidation still causes some damage propagation into the Si substrate [27], it has been used to improve the performance of perforated devices by a considerable factor (after selective doping) [21]. Yet, postprocess oxidation consumes the Si

[1] The effective range, as described in [6], refers to the maximum range a particle has before dropping below a designated energy. For instance, the maximum range of a 1.47 MeV alpha particle in pure ^{10}B is 3.6 μm, yet the effective range with the LLD = 300 keV is only 2.65 μm.

substrate at a ratio of 0.46 of the total oxide thickness, thereby removing the Si surface damage. In previous work, the amount of Si removed from the sidewall surfaces amounted to approximately 250 nm [21], although there is indication that considerable improvement can be achieved with Si consumption as low as 13 nm [26]. Regardless, postprocess oxidation further limits the minimum feature size of the perforations and must be considered when designing the structures. The SiO_2 acts as a insensitive region to the reaction products and reduces their energies before reaching the semiconductor, hence the effective intrinsic thermal-neutron detection efficiency is reduced.

The backfilling of neutron reactive materials poses a problem with destruction of the rectifying boundaries. The two most attractive materials for backfilling are forms of ^{10}B and ^{6}Li. The isotope ^{6}Li is reactive and difficult to prevent from decomposing, hence, it is the stable compound ^{6}LiF that is generally used. Unfortunately, in Si, ^{10}B is a p-type dopant and ^{6}Li is an n-type dopant. If the materials are applied in the perforations or around the pillars at elevated temperatures, they can, and most likely do, inadvertently dope the sidewalls of the structures and destroy the rectifying properties of the device's pn junctions. Both ^{10}B and ^{6}LiF can be applied with physical vapor deposition, a process that tends not to dope the surfaces; however, the process is self-limiting, in that the holes become prematurely plugged before being completely filled [5]. Chemical vapor deposition is typically done at elevated temperature, hence there is a danger of unintentionally doping the sidewalls with this process. Finally, at elevated temperatures, LiF is reactive and etches SiO_2 and can destroy the oxide region used to reduce leakage current and, hence, destroys the structure. As a result, a room-temperature or low-temperature method of depositing the neutron reactive materials in the perforations is needed. One such technique has been proposed by McGregor [28,15].

It was found that through-junction etching damages the rectifying properties of the device. By maintaining a minimum 3-μm buffer region between the etch boundary and the actual junction location, the leakage current can be reduced by an order of magnitude [21]. In the reported work, ^{6}LiF backfilled devices fabricated with 30-μm-diameter holes were surrounded by dopant blocking patterns with at least 36-μm-diameter patterns centered over the holes [21]. Yet, due to lateral diffusion during doping and activation, the actual patterned dopant blocking region is larger, producing 38-μm-diameter blocking patterns for the initial doping regions before diffusion and drive-in. The same criteria are needed for trenches and pillars. For 30-μm-wide trenches, the dopant pattern would be 22 μm wide centered on the Si fins, and for 30-μm-diameter pillars, the dopant pattern would be represented by 22-μm-diameter regions centered atop the pillars. It thus becomes obvious that 2-μm-diameter pillars and 2-μm-wide trench structures could not be produced with such a procedure, as there is simply not enough material to work with. In fact, the buffer region would have to be less than 1 μm wide before 2-μm pn junction features could be made, and such small features are impractical due to physical constraints. Hence, the small structure dimensions suggested elsewhere are simply impractical and most likely will not result in viable detectors [8,17]. Finally, it might be possible to use the conformal diffusion process to help remedy the issue, in which case the dead region surrounding the perimeter of the pillars might be reduced [13]. As a result, the pillars and trenches could be made with smaller features, yet the feature size will still be predetermined by the diffusion depth of the junction dopants and the required material to absorb enough energy from the reaction products.

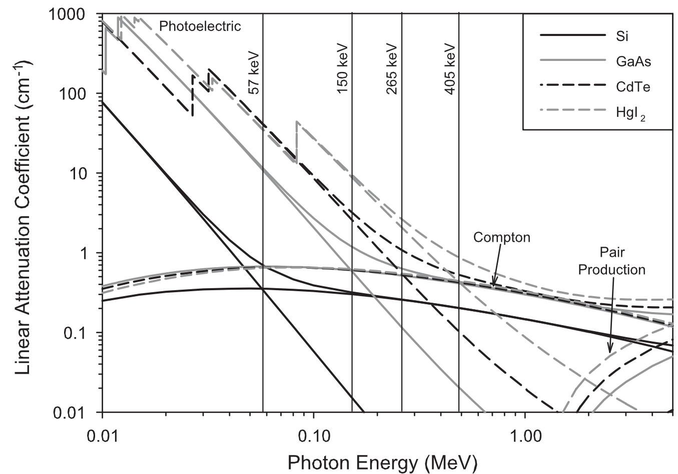

Fig. 84. The photon cross sections for several materials, showing the contributions from photoelectric absorption, Compton scattering and pair production. Note that the contributions from photoelectric absorption and Compton scattering are equal at 58, 150, 265, and 405 keV for Si, GaAs, CdTe and HgI_2, respectively [29].

4.3. Noise and background

Background counts, electronic noise, and device imperfections require that the LLD setting be sufficiently high to discriminate spurious and background counts from neutron-induced counts. From previous analyses [7], LiF-filled devices retain higher efficiencies than ^{10}B-filled devices as the LLD setting is increased, making it the more attractive converter material. The reason for the efficiency retention is due to the higher energy reaction ions produced by the $^{6}Li(n,t)^{4}He$ reaction compared to those from the $^{10}B(n,\alpha)^{7}Li$ reaction. Hence, it is expected that a device that utilizes ^{6}LiF rather than ^{10}B as the converter can be operated in mixed radiation fields with higher confidence that neutron counts are being distinguished from background gamma-ray events.

4.4. Substrate choice

Choice of substrate for microstructured semiconductor neutron detectors also affects performance. Two salient aspects of the semiconductor are important, mainly, the substrate should be as transparent as possible to photons and neutrons. Material cost is also a concern, and often can be prohibitive. Reduction of photon interactions in the detector is accomplished by (a) choosing substrate materials composed of low Z materials and (b) minimizing the thickness of the substrate. Of the most common commercially available semiconductors, Si stands out as the obvious candidate. With a Z of 14, Si has a low photon interaction probability for photoelectric and Compton scattering. Other low Z semiconductors, such as SiC and diamond, are expensive and difficult to process compared to Si and, hence, are less attractive as a low cost candidate for mass produced neutron detectors.

Fig. 84 shows the cross sections for photon interactions in Si [29]. Notice that the photoelectric effect dominates those interactions at photon energies below 57 keV. Above 57 keV, Compton scattering becomes the dominant interaction and remains so up to relatively high energies (above 10 MeV) before pair production dominates. For good neutron detection, it is important that events recorded in the detector are not photon induced background counts mistakenly accepted as neutron counts. The probability of such a misinterpretation can be reduced by setting the LLD at a sufficiently high channel so high energy photons have less of a chance of being recorded as a count. For instance, an LLD setting greater than 57 keV will ensure that

Table 7
Thermal neutron cross section (b) for common semiconductors [30].

Semiconductor	Z numbers	Absorption	Scattering
C (diamond)	6	0.0035	5.55
SiC	14/6	0.16/0.0035	1.7/5.55
Si	14	0.16	1.7
Ge	32	2.2	8.6
GaAs	31/33	2.75/4.5	6.83/5.5
InP	49/15	193.8/0.172	2.62/3.31
CdTe	48/52	2520/4.7	6.5/4.32
CdZnTe	48/30/52	2520/1.11/4.7	6.5/4.13/4.32
HgI_2	80/53	372.3/6.15	26.8/3.81
PbI_2	82/53	0.171/6.15	11.11/3.81

Compton scattering will dominate photon interactions in Si. If the LLD is set to 300 keV, then photons must have an energy of at least 465 keV to deposit enough energy to be registered because Compton scattered photons cannot deposit their full energy.[2] Further, if the LLD is raised to 500 keV, then photons must have at least 685 keV of energy in order to deposit at least 500 keV of energy in the device. By keeping the Si substrate thin, the probability of reabsorbing the Compton scattered photon is small. Additionally, Compton events are predominantly forward scattered as the initial gamma-ray energy increases; hence the probability that a photon will backscatter and deposit the maximum (or nearly maximum) amount of energy to a Compton electron decreases with increasing photon energy, further diminishing the probability of recording a background photon event. Finally, photoelectrons or Compton electrons with energies greater than 65 keV have transit lengths in Si of 40 μm or greater, a dimension larger than the lateral dimensions of the ^{6}LiF device features discussed in the present work. By keeping the Si substrate thin, the probability of reabsorbing the Compton scattered photon is small. Hence, even if an event occurs that produces an energetic electron of 500 keV or greater to be emitted in the Si substrate, it is unlikely that it will deposit enough energy in the substrate to exceed a 500 keV LLD setting and be recorded.

The thermal-neutron (n,γ) cross section for Si is only 0.16 b and the scattering cross section is 1.7 b. These values indicate that direct interactions or absorptions in the thin Si substrate are improbable. However, such reactions become important for stacked detector configurations, in which it is important that those neutrons that do not interact in the neutron absorption converter material of the first device in the stack pass through the semiconductor material of the device unperturbed to possibly interact in the reactive material of an adjacent device in the stack. For instance, if a CdTe substrate is used, one can expect that those neutrons not interacting in the neutron reactive converter materials in the micro-structures will be readily absorbed in the Cd of the substrate, hence will not pass through to the next detector for possible detection.

In Fig. 84 a comparison of photon cross sections for several different commonly available semiconductor substrate materials is shown. This comparison clearly shows Si is the best choice to avoid photon background interference. Also a comparison of neutron absorption and scattering cross sections for numerous possible semiconductors (see Table 7) again reveals that Si has the lowest thermal-neutron interaction cross sections, even lower than C and SiC. Hence, after considering cost, availability, photon interference, and neutron absorption or scattering, it becomes clear that Si is best choice for a micro-structured semiconductor neutron detector.

4.5. *Stacked configurations*

The efficiency of the compact devices can be greatly improved by stacking micro-structured devices [6,16]. In the best case, the front device converter will not shadow the converter of the second device. Otherwise, the stacking is less effective. As it turns out, of the three geometries discussed in this paper, only the trench design can be stacked such that the front device converter does not shadow the second device converter while still allowing for the sum of the converter areas to completely fill the total detector area. Hence, the efficiency can be doubled for trench devices. This doubling cannot be realized for the cylindrical pillar design considered here because a majority of incident area in the first device is covered by converter, thereby, blocking neutrons from reaching the offset semiconductor areas of the second device. The cylindrical hole design also does not stack well, but the efficiency can still be doubled, mainly because neutrons are shadowed only by the holes in the first substrate, and the second substrate holes can be aligned with the spaces between first substrate holes. A permutation of the hole (or trench) design is the possibility of producing a "checkerboard" pattern, which would allow for non-shadowed stacking. Although not analyzed in the present work, the checkerboard pattern will have feature compromises between the pure hole and pure straight trench design. Unfortunately, the issues of neutron streaming at select incident angles will still be present.

5. Conclusions

Based on the results and observations presented here, the following can be stated:

1. The effective ranges of the reaction products from the ^{6}Li(n, t)^{4}He reaction are much greater than the effective ranges of reaction products from the ^{10}B(n, α)^{7}LiF reaction. Hence, the microstructured features for ^{6}LiF-filled devices can be larger than the features in a ^{10}B-filled device, with the consequence that the ^{6}Li-filled device features must be deeper. Further, semiconductor processing chemistry and physics place limits on the minimum features that can be fabricated (B-filled devices are already approaching that limit but this is not the case for ^{6}LiF-filled devices). Hence, it appears that ^{6}LiF filled devices are more forgiving to manufacture.
2. Si appears to be the best choice as a substrate, mainly because Si has low gamma-ray and neutron interaction cross sections, thereby reducing background radiation interactions in the semiconductor detector. Further, Si processing technology is very mature.
3. At low LLD settings and minimal feature sizes, the pillar design has the highest efficiency. However, with the LLD set at channels generally necessary to discriminate against background photons, the trench design out performs the other designs. As the feature sizes are increased, the trench design has the best efficiency at all LLD settings. The hole design has the lowest efficiency for all cases.
4. The hole design shows the highest stability as a function of LLD setting with minimal changes observed for LLD settings ranging from 0 to 600 keV for ^{6}LiF filled devices. The pillar design shows the largest change in efficiency as a function of the LLD.

[2] The maximum energy transferred to a Compton electron (E_c) from a Compton scattered photon is $E_c = E_\gamma - (E_\gamma/[1 + E\gamma/255.5\,\text{keV}])$ where E_γ is the initial gamma ray energy. Hence, the highest possible energy deposited by a Compton scattered 465 keV gamma ray is only 300 keV.

5. Higher efficiency can be achieved by stacking the semiconductor detectors. The efficiencies for trench and hole devices can be doubled, whereas the efficiency for pillar devices will increase only slightly due to neutron absorption in the first device in the stack.

Hence, it appears that stacked micro-structure devices with a trench style design backfilled with ^{6}LiF offers the overall best design for efficiency, background discrimination, and fabrication. Variants on the trench design have been reported, which include sinusoidal trenches and long linear pixels with straight trenches [9,22,23]. The sinusoidal trench designs offers a much more uniform response to neutrons over that of the pillar, hole, and straight trench designs. Currently long linear pixel devices are being investigated as high-resolution neutron-detection arrays.

References

[1] Neutron Detectors, International Atomic Energy Agency, Bibliographical Series, no. 18, Vienna, 1966.
[2] R.L. Schulte, F. Swanson, M. Kesselman, Nucl. Instr. and Meth. A 353 (1994) 123.
[3] D.I. Garber, R.R. Kinsey, BNL 325: Neutron Cross Sections, third ed., vol. 2, Curves, Brookhaven National Laboratory, Upton, 1976.
[4] V. McLane, C.L. Dunford, P.F. Rose, in: Neutron Cross Sections, vol. 2, Academic Press, San Diego, 1988.
[5] D.S. McGregor, R.T. Klann, H.K. Gersch, E. Ariesanti, J.D. Sanders, B. Van Der Elzen, IEEE Trans. Nucl. Sci. NS-49 (2002) 1999.
[6] D.S. McGregor, M.D. Hammig, H.K. Gersch, Y.-H. Yang, R.T. Klann, Nucl. Instr. and Meth. A 500 (2003) 272.
[7] J.K. Shultis, D.S. McGregor, IEEE Trans. Nucl. Sci. NS-53 (2006) 1659.
[8] R.J. Nikolic, C.L. Cheung, C.E. Reinhardt, T.F. Wang, Roadmap for high efficiency solid-state neutron detectors, in: Proceedings of the SPIE, Photonics West, Boston, MA, 2005.
[9] C.J. Solomon, J.K. Shultis, W.J. McNeil, T.C. Unruh, B.B. Rice, D.S. McGregor, Nucl. Instr. and Meth. A 580 (2007) 326.
[10] J.K. Shultis, R.E. Faw, Radiation Shielding, American Nuclear Society, La Grange Park, Illinois, 2000.
[11] J.F. Ziegler, J.P. Biersack, Transport of Ions in Matter in SRIM-2003 Code, Version 26 (www.srim.org) (IBM Corporation, 2003).
[12] Jandel Scientific, Table Curve, version 3.0, Curve Fitting Software, Jandel Scientific, Corte Madera, CA, 1991.
[13] D.S. McGregor, J.K. Shultis, Nucl. Instr. and Meth. A 517 (2004) 180.
[14] D.S. McGregor, R.T. Klann, Patent US-6545281, allowed April 8, 2003.
[15] D.S. McGregor, S.L. Bellinger, D. Bruno, W.J. McNeil, E. Patterson, J.K. Shultis, C.J. Solomon, T. Unruh, Proc. SPIE 6706 (2007) 0N1.
[16] D.S. McGregor, R.T. Klann, Patent US-7164138, allowed January 16, 2007.
[17] R.J. Nikolic, C.L. Cheung, C.E. Reinhardt, T.F. Wang, Future of semiconductor based thermal neutron detectors, in: Proceedings of the NSTI Nanotech 2006, Boston, MA, 2006.
[18] H. Matasumoto, T. Sugano, J. Electrochem. Soc. 129 (1982) 2823.
[19] A. Henry, O.O. Awadelkarim, J.L. Linstrom, G.S. Oehrlein, J. Appl. Phys. 66 (1989) 5388.
[20] A. Belkacen, E. Andre, J.C. Oberlin, C. Pomot, P. Pajot, A. Chantre, Mater. Sci. Eng. B 4 (1989) 451.
[21] W.J. McNeil, S. Bellinger, T. Unruh, E. Patterson, A. Egley, D. Bruno, M. Elazegui, A. Streit, D.S. McGregor, in: Conference Record of the IEEE Nuclear Science Symposium, San Diego, CA, October 29–November 3, 2006.
[22] W.J. McNeil, S.L. Bellinger, B.J. Blalock, C.L. Britton Jr., J.L. Britton, S.C. Bunch, W.L. Dunn, C.M. Henderson, T.J. Sobering, R.D. Taylor, T.C. Unruh, D.S. McGregor, in: Conference Record of the IEEE Nuclear Science Symposium, Waikiki, Hawaii, October 28–November 3, 2007.
[23] S.L. Bellinger, W.J. McNeil, T.C. Unruh, D.S. McGregor, in: Conference Record of the IEEE Nuclear Science Symposium, Waikiki, Hawaii, October 28–November 3, 2007.
[24] D.S. McGregor, S.L. Bellinger, W.J. McNeil, T.C. Unruh, in: Conference Records of the IEEE Nuclear Science Symposium, Dresden, Germany, October 19–25, 2008.
[25] W.J. McNeil, S. Bellinger, T. Unruh, D.S. McGregor, Nucl. Instr. and Meth., 2009, submitted for publication.
[26] W. Wu, P.K. McLarty, J. Vac. Sci. Technol. A 13 (1995) 67.
[27] S.W. Pang, D.D. Rathmnan, D.J. Silversmith, R.W. Mountain, P.D. Degraff, J. Appl. Phys. 54 (1983) 3272.
[28] D.S. McGregor, S.L. Bellinger D. Bruno, S. Cowley, M. Elazegui, W.J. McNeil, E. Patterson, B.B. Rice, C.J. Solomon, J.K. Shultis, T. Unruh, in: Conference Record of the IEEE Conference on Technologies for Homeland Security, Woburn, MA, May 16–17, 2007.
[29] NIST Physics Laboratory, Physical Reference Data, XCOM (http://physics.nist.gov/PhysRefData/Xcom/html/xcom1.html), December 1, 2008.
[30] NIST Center for Neutron Research (http://www.ncnr.nist.gov/resources/n-lengths/), December 1, 2008.